Water-Responsive 3D Electronics for Smart Biological Interfaces

Yuanyuan Cui,[¶] Lizhu Li,[¶] Changbo Liu,* Yuqi Wang, Mengwei Sun, Ben Jia, Zhangming Shen, Xing Sheng,* and Yuan Deng*

ACCESS | Metrics & More | Article Recommendations | Supporting Information

ABSTRACT: Three-dimensional (3D) electronic systems with their potential for enhanced functionalities often require complex fabrication processes. This paper presents a water-based, stimuli-responsive approach for creating self-assembled 3D electronic systems, particularly suited for biorelated applications. We utilize laser scribing to programmatically shape a water-responsive bilayer, resulting in smart 3D electronic substrates. Control over the deformation direction, actuation time, and surface curvature of rolling structures is achieved by adjusting laser-scribing parameters, as validated through experiments and numerical simulations. Additionally, self-locking structures maintain the integrity of the 3D systems. This methodology enables the implementation of spiral twining electrodes for electrophysiological signal monitoring in plants. Furthermore, the integration of self-rolling electrodes onto peripheral nerves in a rodent model allows for stimulation and recording of in vivo neural activities with excellent biocompatibility. These innovations provide viable paths to next-generation 3D biointegrated electronic systems for life science studies and medical applications.

KEYWORDS: stimuli-responsive, laser scribing, programmable deformation, 3D electronics, biological interfaces
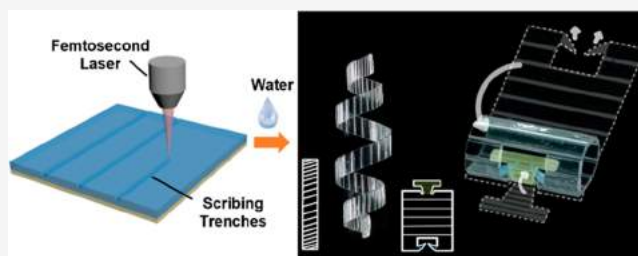
Three-dimensional (3D) electronics revolutionize micro-systems technology,[1,2] opening the door to innovative applications such as 3D functional biological interfaces.[3−5] Biological interfaces, crucial in bridging biological systems and synthetic materials, play a central role in biological science.[6] However, conventional electronics typically fabricated on flat and rigid substrates fall short in adapting to the complex 3D curved surfaces in biological systems.[7] Most flexible electronic devices that rely on soft materials, ultrathin structures, or adaptive structures need additional fixation using adhesive tape or viscous hydrogel, posing harm to organisms and degumming risks in biological fluids.[8−10] 3D direct manufacturing methods such as additive manufacturing, spraying, and thermal forming[11−15] are suitable for limited materials and electronic devices, thus lacking universality, and additional three-dimensional processing techniques are required, limiting application in organisms due to potentially harmful processes.

Stimuli-responsive deformable substrates offer a promising solution for 3D electronics,[2] allowing the integration of electronic devices in a planar state, transforming into 3D structures upon stimulation. This approach achieves self-mounting and self-fixing of devices on 3D surfaces, enabling compatibility with 2D microsystems and scalability and minimizing harm during device preparation and installation in 3D functional biological interfaces.

Previous reports have established several stimuli-responsive deformable biological interfaces (Table S1). However, they have limitations in precise deformation control for achieving 3D shape predesign. Shape-memory polymers require preprogrammed shapes using molds, limiting design flexibility and complexity.[16−20] Flex resin or hydrogel patterned by photolithography or other methods usually needs complex or time-consuming processes.[21−24] Temporal dimension control in these schemes is challenging, limiting their use in sophisticated shape-shifting structures. Direct integration of microelectronic devices on these substrates is hindered by material constraints or scalability issues.

We aimed to provide a smart substrate for 3D biological interfaces with dynamic deformation control. To this end, we established a laser-scribing programmed water-responsive shape-shifting bilayer. This bilayer consists of a super absorbent poly(vinyl alcohol) (PVA) active layer providing a large actuating force to drive the functional layer with considerable thickness and stiffness and a polycaprolactone (PCL) passive layer compatible with microelectronics through 2D manufacturing processes. Both materials boast excellent biocompatibility and biodegradability, and the bilayer can naturally dissolve and degrade in the animal body,[25−28] thus
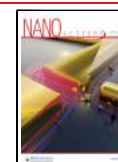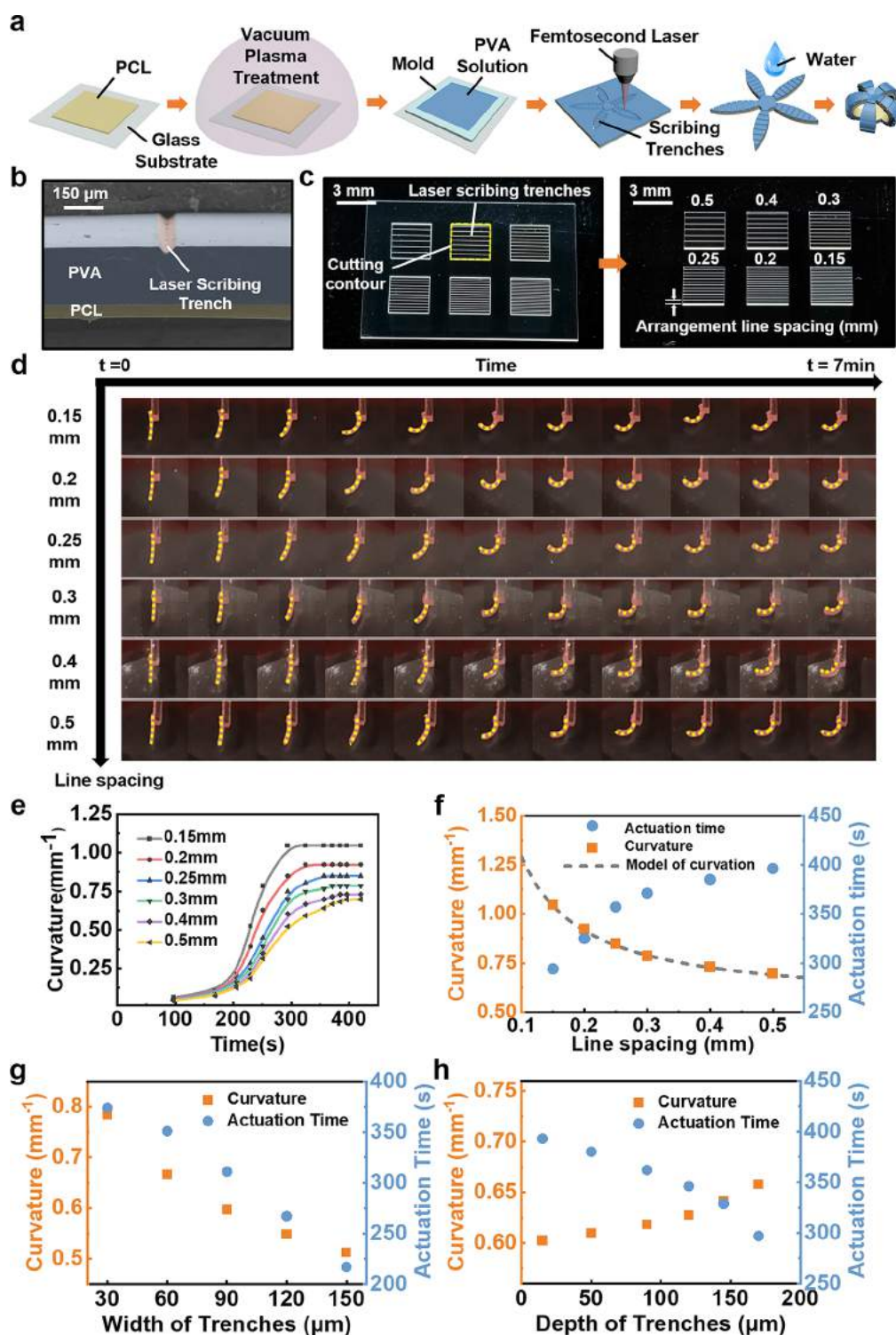
Figure 1. Laser scribing programmed shape-shifting bilayers. (a) Fabrication process of the bilayer with laser-scribing trenches and its directional shape-shifting. (b) Scanning electron microscopic (SEM) image (cross-sectional view) of a single scribing trench. (c) Optical images of the bilayers with different directional arrangement line spacing of scribing trenches. (d) Deformation process of bilayers with different line spacing of scribing trenches. (e) Statistics of the curvature of bilayers with different line spacing over time. (f) Quantitative analysis of experimental dependence of curvature and actuation time on line spacing of scribing trenches and model analysis of curvature. (g) Dependence of curvature and actuation time on the width of scribing trenches. (h) Dependence of curvature and actuation time on depth of scribing trenches.

possessing the potential for use in biologically and environmentally friendly transient electronics and medical applications.[29] Laser scribing on the active layer dictates the deformation direction, curvature, and actuation time. By adjustment of the deformation parameters in a regional manner, a series of 3D shapes have been assembled, including a predefined self-locking structure. We briefly demonstrate two applications in electrophysiological monitoring and intervening using our shape-shifting bilayers as smart substrate driving electrodes. Precise deformation direction and curvature
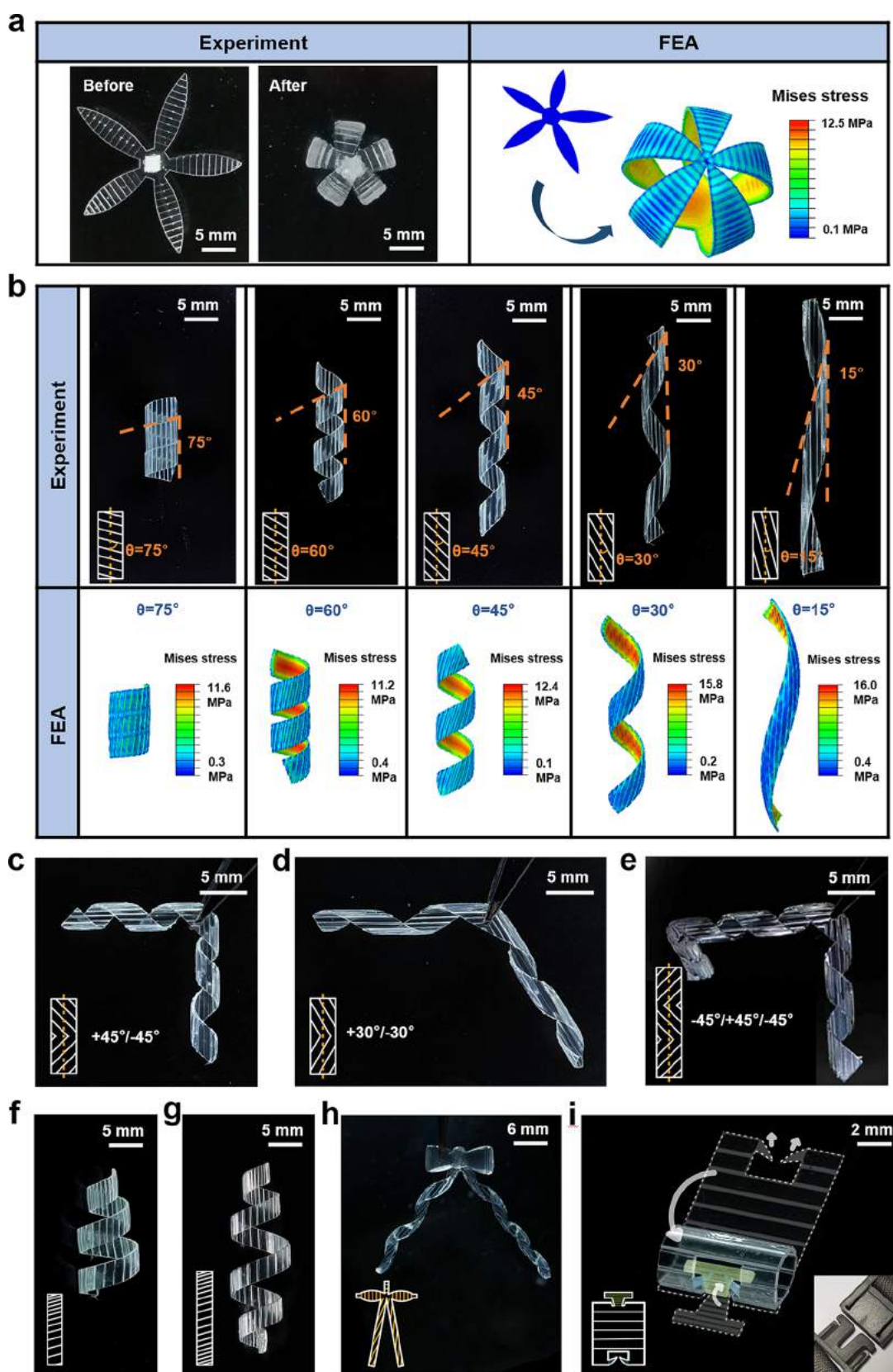
Figure 2. Control of the complex directional shape-shifting of bilayers by laser-scribing trenches. (a) Experiment and simulation of the shape change of a flower. (b) Experiment and simulation of samples with tilt angles of $\theta = 15°$, $30°$, $45°$, $60°$, and $75°$ are shown. (Tilt angle (θ) is defined by the angle between the ribbon axis and the stripes on the top surface). (c−e) Three-dimensional structure composed of successive cylindrical helices in different directions along a straight ribbon. (f,g) Helices with gradually changing radius. (h) Formation of bowknot shape. (i) Snap-fit design inspired self-locking structure.

regulation allow substrates to be flexibly applied to three-dimensional surfaces. The excellent biocompatibility and mechanical properties of the bilayer minimize damage to biological tissues.

Figure 1a schematically demonstrates the fabrication process of the shape-shifting bilayers. The preparation starts with spin-casting of a layer of PCL film onto a glass substrate. The surface of the PCL film is treated with an O_2/Ar_2 plasma to increase the bonding force between the two films, and then the PVA solution is cast into the mold and dried. After the two layers of polymers are prepared, a series of trenches are scribed on the surface of the PVA layer by laser processing, and the contour of the initial two-dimensional shape is also cut by laser to obtain the designed sample. PVA has a strong absorption coefficient in the ultraviolet band so that it can be milled by a laser in the ultraviolet band (Figure S3a). At the same time, the transmission of visible and infrared light gives it advantages in biomedical applications, as it allows for direct observation of the surface of organisms or organs and the state of integrated devices through the bilayer structure and makes the bilayer suitable for integrating functional devices that are remotely operated by infrared light. The laser process is simple and fast, usually taking only a few seconds to a few minutes. A single scribing trench is a V groove (Figure 1b). The dimensions of the scribing trenches can be regulated by adjusting the parameters of the laser processing (Figure S4).

PVA undergoes isotropic hygroscopic expansion in a humid environment with a linear swelling ratio of 0.7 (Figure S1 and Note S2), while PCL is hydrophobic[30,31] and hardly absorbs water (Figure S2 and Note S2), inducing a large strain mismatch when the bilayer encounters humidity stimulation and resulting in deformation. Due to the reduction of the section moment of inertia at the scribing trenches site, the bending stiffness will decrease, and the bending will preferentially follow the direction of trench arrangement.

The bending parameter adjustment of shape-shifting bilayers is usually achieved by changing the thickness ratio, modulus ratio, or swelling rate ratio.[32,33] In our study, quantitative control of the curvature and actuation time is conveniently achieved by laser-scribing trenches.

For the experiment on the influence of arrangement line spacing of trenches, a series of samples with the same dimension (3 mm × 3 mm) and thickness composition (PVA 180 μm, PCL 70 μm) are scribed with laser-induced trenches which have the same depth (100 μm), width (30 μm), and different arrangement line spacing of 0.15−0.5 mm (Figure 1c). The actuation time is defined by the time to reach maximum curvature for samples. The deformation process of samples with different trench line spacings is shown in Figure 1d, and the bending curvature over time of these samples is statistically analyzed in Figure 1e. Significant differences can be seen in the action history of samples with different line spacings. As the line spacing of scribing trenches decreases from 0.5 to 0.15 mm, the curvature of the bilayer curling action gradually increases from 0.698 to 1.047 mm^{-1} (orange symbols in Figure 1f). That is because the proportion of tiny laser-induced damage to the overall PVA film can be almost negligible, while hinge-like fold deformation forms due to the decrease of bending stiffness induced by laser-scribing trenches. A mechanical model where the curvature is adjusted by the line spacing of scribing trenches is established, and the modeling results are highly consistent with the experimental observations (Figure 1f, Figure S5, and Note S4). The

actuation time of the bilayer decreases from 396 to 294 s as the line spacing of scribing trenches decreases (blue symbols in Figure 1f), which may be due to the increase of PVA water absorption surface area and the decrease of the overall bending stiffness of the film. The width and depth of the laser scribing trench can also be adjusted to control bending parameters (Figure 1g, 1h and Note S5). By simultaneously adjusting different parameters of laser-scribing trenches, the actuation time and curvature can be controlled separately (Figure S6 and Note S5).

Complex shapes can be obtained by easily importing CAD data to plan the laser beam path.[34] As is shown in Figure 2a, a flower shape bilayer can be easily obtained through drawing design, and petals curl up, taking the direction of the laser-scribing trenches as the axis by encountering water stimulation. The deformation results predicted by our FEA model are in excellent agreement with experimental observations (Figure 2a and Note S6).

To verify the precise controllability of laser-scribing trenches on the action of shape-shifting bilayers, we obtained different helix shapes by adjusting the arrangement direction of laser-scribing trenches on strip samples with identical thickness compositions and dimensions (Figure 2b). The angle between laser-scribing trenches and the long side of the strip is defined as θ. Samples with tilt angles of $\theta = 75°$, $\theta = 60°$, $\theta = 45°$, $\theta = 30°$, and $\theta = 15°$ are shown in Figure 2b. The CAD drawings of laser processing are displayed in the insets of each subplot. The results obtained from the experimental tests show that the curling direction can be controlled precisely. The helix angle of samples is equal to θ, with the error within $\pm 3°$. This error can be further reduced by optimizing the fabrication process of bilayers to improve their uniformity or optimizing laser processing parameters. The FEA simulation model we established also accurately predicts the deformation actions (Figure 2b).

Three-dimensional concatenated structures containing multiple helical segments are obtained by conducting a regional distribution of different scribing trench arrangement directions on samples (Figure 2c−e and Movie S1). The angle between each two segments depends on the angle between the scribing trenches of two areas. Helix shapes with diverse curvature at different areas including a conical helix with a gradually decreasing radius R (Figure 2f) and a helix with large middle and small ends (Figure 2g) are obtained by conducting regional distribution of different directional arrangement line spacings of scribing trenches.

More sophisticated 3D shapes can be achieved by ingeniously combining the regional distribution design of scribing trench arrangement directions and line spacing. As an example, a self-assembled bowknot shape is obtained by regulating the actions of various parts (Figure 2h and Movie S2). Inspired by snap-fit joints which are a type of mechanical fastener for joining two parts together,[35−37] we developed a self-locking structure that can fix the curvature of the structure (Figure 2i and Movie S3). The CAD drawings of laser processing are displayed in the insets. The precise cooperation of deformation in different parts of the bilayer in both temporal and spatial dimensions is the key to the successful assembly of the self-locking structure (Note S7). Several self-locking structures with different self-locking curvatures from 0.4 mm^{-1} to 1.3 mm^{-1} are obtained on one film, and they are arranged into different patterns through bending actions at the connections of two self-locking structures (Figure S8). By
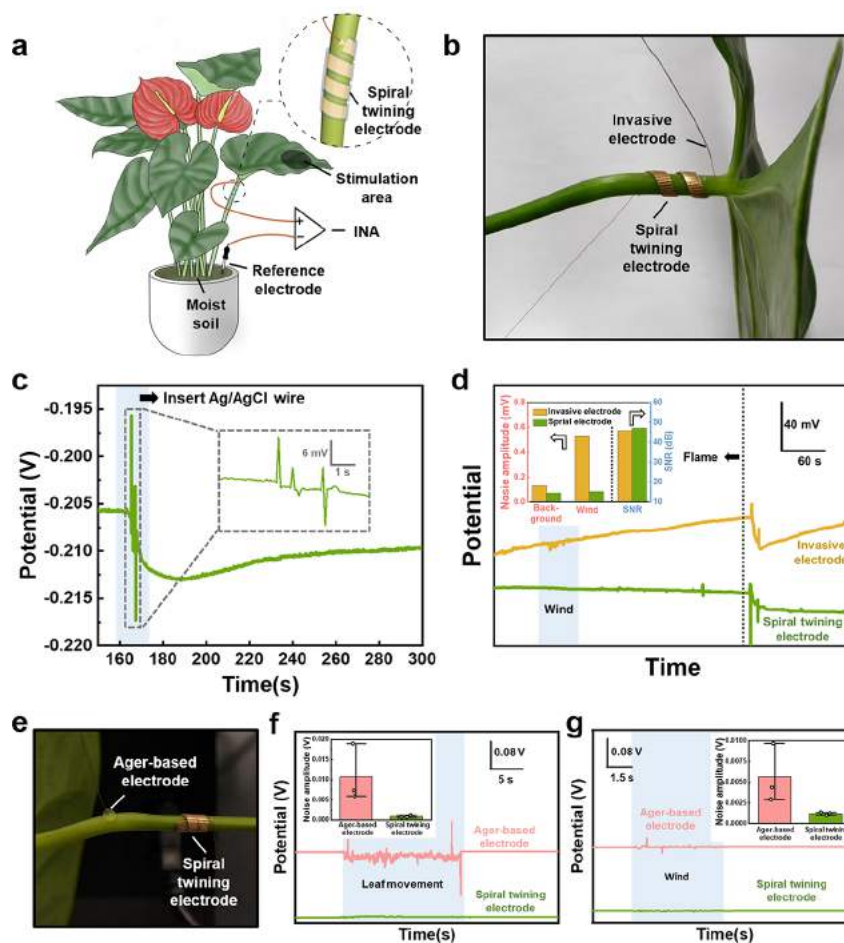
Figure 3. Noninvasive monitoring of potential signals in plants by spiral twining electrodes. (a) Schematic showing the setup for the experiments. INA, instrumentation amplifier. (b) Optical images showing spiral twining electrodes and invasive electrodes mounted on plants. (c) Potential signal due to injury caused by mounting an invasive electrode recorded with the spiral twining electrode. (d) Signals from the electrodes in b in a flame-wounding experiment. Blue shading indicates periods of mechanical disturbance. Inset displays the quantified comparison of signal quality between the two electrodes (root-mean-square (rms) background noise amplitude, rms wind noise amplitude, wounding signal to background noise ratio (SNR)). (e) Optical images showing spiral twining electrodes and ager-based electrodes mounted on plants. (f,g) Signals from the electrodes in g in mechanical interference experiments. Blue shading indicates periods of mechanical disturbance. Inset displays quantified comparison of signal quality between the two electrodes (root-mean-square (rms) noise amplitude).

designing the components to different positions of the self-locking structure, we can obtain any curvature smaller than the original curvature of the bilayer. This large curvature regulation range enables the bilayer to be suitable for target objects of multiple sizes. In addition, the self-locking structure can provide a certain confinement force to prevent the bilayer from falling off from the target object and to maintain good interface contact, which has a certain significance for application in the field of conformal electronics.

The strategy of laser direct writing microstructures to control the deformation of bilayers is simple, efficient, and scalable. It allows for the generation of mechanical nonuniform fields that lead to anisotropic deformation without changing the intrinsic properties of the material (such as cross-linking density, Young's modulus, etc.) and can therefore be extended to other deformation systems (Note S16 and Figure S9). The smallest 3D assembly structure that has ever been made using our PVA/PCL shape-shifting bilayer is a cylinder with an inner diameter of approximately 100 μm and an outer diameter of approximately 200 μm (Figure S13), and the smallest feature size achievable by this 3D assembly method should be less than this size.

Herein, we briefly demonstrate two applications in 3D functional biological interfaces based on our shape-shifting bilayers, respectively, in the field of plant electrophysiology research and animal neural interfaces.

Electrical signals count for much for plants to perceive and respond to the environment. Monitoring and even interfering with plant electrophysiological signals through advanced electronic technology have potential benefits for food supply and ecological environment protection.[38−42] We report a spiral twining electrode for plant electrophysiological monitoring with the capability of self-crimping driven by humidity and the formation of a solid conformal interface. The preparation process of the spiral twining electrode is shown in Figure S10 and Note S8. Spiral twining electrodes in a flat state will climb and twine the plant stem independently and conformally like vines when encountering humidity stimulation. The cylindrical spiral radius of twining electrodes is designed to match the plant stem to ensure a solid conformal interface and no restraint damage to the plant stem. Due to the small elastic modulus of PVA in the swelling state, the dehydration of PVA cannot drive the bilayer to restore its original shape, so the

electrode maintains its shape even after dehydration (Figure S12).

To demonstrate that the spiral twining electrode can stably and high-fidelity monitor plant electrophysiological signals, we record the flame-induced variation potential of *Anthurium andraeanum*. The schematic diagram of the setup is shown in Figure 3a. The installation process of the spiral twining electrode is simple (Movie S4). The traditional Ag/AgCl invasive electrode is selected as the control electrode (Figure 3b). Figure 3c shows the electrical signal generated by plants during the installation of the Ag/AgCl invasive electrode recorded by the spiral twining electrode. A variation potential of approximately 8 mV is detected due to the damage to plants caused by the inserted metal electrode.

As shown in Figure 3d, when there is external mechanical disturbance, such as wind, spiral twining electrodes can maintain a stable signal baseline, and the noise has an average amplitude of 85 μV, which is much smaller than the average noise amplitude of about 526 μV recorded by the invasive electrode. When a leaf is burned by flames, the spiral twining electrode can accurately record the variation potential just like the invasive electrode.

To prove the ability of the spiral twining electrode to resist mechanical disturbance and obtain a stable signal, the spiral twining electrode and traditional agar-based surface electrode are used to monitor the electrophysiology of *Anthurium andraeanum* and compared in terms of the noise generated by shaking plant leaves and blowing plants, which are used to simulate external environmental disturbances in nature. The photo of the setup is shown in Figure 3e. As shown in Figure 3f and 3g, agar-based electrodes recorded obvious interference or large drifts with an average noise amplitude of 10.7 and 5.6 mV when the leaf experienced movements separately by shaking and blowing, which is much greater than the average noise amplitude of about 0.8 and 1.2 mV recorded by the spiral twining electrode, as a result of the unstable interface between agar gel and plants. The spiral twining electrodes obtain high-quality signals and have strong anti-interference ability compared to agar-based electrodes. The spiral twining electrode is proven to have application potential in plant electrophysiological testing and provided an idea for the design of plant electrophysiological surface electrodes.

The peripheral nervous system (PNS) is the routing system of the body.[43] Direct monitoring and intervention of the peripheral nervous system is a solution to nervous system diseases.[44−49] Several extraneural electrodes have been developed for peripheral nerve interfaces.[19,50−55] One problem is mechanically induced neural damage due to possible mechanical and geometrical mismatches. It is necessary to accurately control the shape and dimensions of the 3D neural interface and avoid additional surgical fixation. Herein, we develop a self-rolling electrode with a self-installation function, shape adaptability, mechanical fitness, and biocompatibility for peripheral nerve stimulation and recording. The preparation process of the self-rolling electrode is shown in Figure S10 and Note S8. The bending radius of the self-rolling electrode is designed to match the nerve to ensure a solid conformal interface. Histological images of the sciatic nerve and surrounding muscle tissue show minimal damage to the tissue and negligible immune response caused by the implantation (Figure 4a). After 3 weeks of implantation, the cellular morphology and the nerve construct are well maintained. Figure 4b and 4c shows the schematic diagram and optical
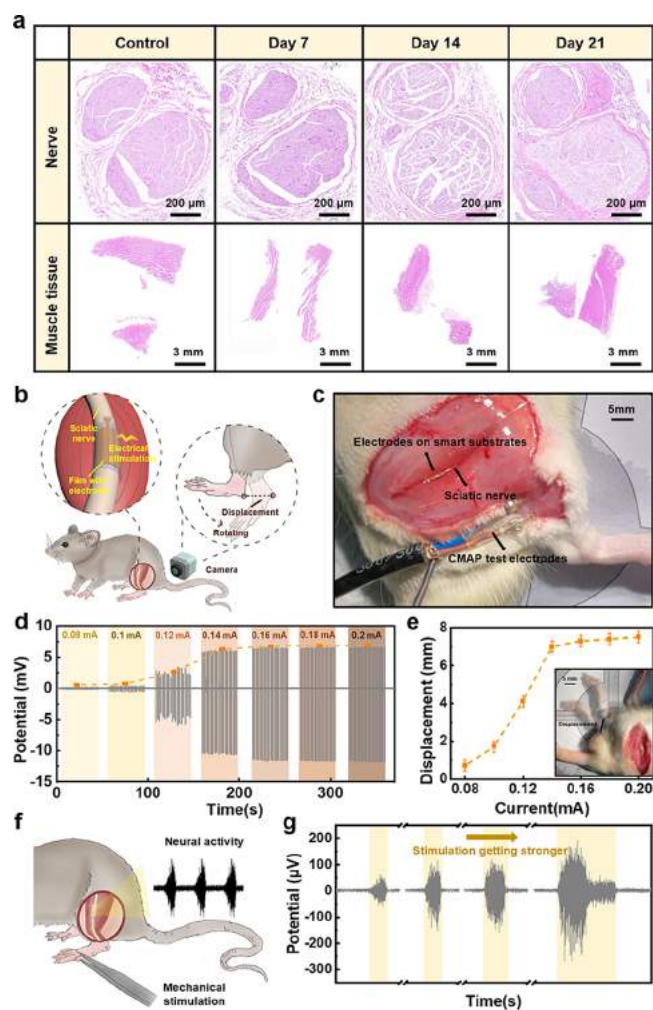
Figure 4. In vivo recording and stimulation of the sciatic nerve of rats using self-deformation electrodes. (a) Hematoxylin and eosin (H&E) stained histological sections of the sciatic nerve and surrounding muscle tissue for rats with films implanted for days 7, 14, and 21. The image for the control sample is from a rat without implants. (b) Schematic showing the setup for the stimulation experiments. Motion tracks are captured by a camera. An external stimulating electrode placed in the proximal position of the nerve evokes hindlimb movements. (c) Optical images showing the self-deformation electrode and the CMAP test electrode mounted on the sciatic nerve. (d) CMAP generated when electrical stimulation uses self-deforming electrodes. (e) Movement of the hindlimb during electrical stimulation using self-deforming electrodes. Inset displays the definition of displacement as well as the unit length. (f) Schematic showing the setup for the recording experiments. Neural activity resulting from mechanical stimulation of hindlimbs is recorded by the self-deformation electrode. (g) Nerve activity resulting from progressively increasing mechanical stimulation of the hindlimbs.

image of in vivo experiments. The prepared self-rolling electrode is placed close to the nerve in a planar state and spontaneously wraps the target nerve under humidity driving, forming a conformal and solid 3D electrode−nerve interface.

The self-rolling electrode is used to stimulate the sciatic nerve of the rat, and the compound muscle action potential (CMAP) evoked due to the cell depolarization is obtained using a commercial CMAP test electrode. As shown in Figure 4d, as the stimulation current of the self-rolling electrode increases from 0.08 to 0.2 mA, the amplitude of the CMAP

gradually increases from 0.17 to 6.55 mV and tends to saturation. When the sciatic nerve is electrically stimulated, regular shaking of the hindlimb of rats is observed (Movie S5). That is because the evoked action potentials are transmitted along the nerve to the motor end plates after the sciatic nerve is electrically stimulated, enabling contraction of the relevant muscles and thus leading to the movement of the hindlimb. The displacement of the calcaneus in the hindlimb during electrical stimulation is statistically shown in Figure 4e. The definition of calcaneus displacement is shown in Figure 4b and the inset of Figure 4e. As the stimulation current of the self-rolling electrode increases from 0.08 mA to 0.2 mA, the displacement of the calcaneus gradually increases from 0.7 mm to 7.5 mm.

The self-rolling electrode is installed and wrapped on the sciatic nerve to record the compound nerve action potentials (CNAPs) generated by mechanical stimulation of the feet of the rat using forceps. The schematic diagram of the setup is shown in Figure 4f. As shown in Figure 4g, the CNAPs are accurately captured by the self-rolling electrode. When the mechanical stimulation gets stronger, gradually enhanced electrical signals can be observed using self-rolling electrodes (Figure 4g and Movie S6), which are consistent with the literature.[56−58]

The developed self-rolling electrodes provide a mechanical and geometrical adaptable peripheral nerve−electrode design solution with simplified surgical implantation and thus show promising potential in both clinical practice and basic neuroscience research.

In conclusion, we developed a water-responsive deformable bilayer for smart 3D biological interfaces with the capability to program control action parameters. Various complex shapes with a strictly controllable deformation direction and quantitatively adjustable deformation curvature have been obtained. The strategy of laser direct writing microstructures to control the deformation of bilayers is simple and efficient and can be extended to other deformation systems. Although the PVA/PCL shape-shifting bilayer does not have the ability to control reversible deformation, there is the potential to break the limitation of irreversible deformation in PVA/PCL bilayer systems by extending to other deformation systems. Shape-adaptable biological electrophysiological electrodes with desirable biocompatibilities are obtained, which can form stable conformal interfaces without any additional fixation and reduce damage caused by complicated surgical implantation in animal electrophysiology, demonstrating the application prospects of this smart substrate in the field of 3D electronics. Due to its compatibility with 2D planar microelectronic processing processes, this smart substrate has good scalability and can be integrated with other microelectronic devices for use in 3D electronics, providing a flexible solution for the design of 3D electronics.

■ ASSOCIATED CONTENT

Ⓢ Supporting Information

The Supporting Information is available free of charge at https://pubs.acs.org/doi/10.1021/acs.nanolett.3c03394.

> Preparation and characterization of PVA, PCL, and PCL films. Laser processing. Modeling the bilayer mismatched expansion structure. Dependence of curvature and actuation time on width of trenches and depth of trenches. Finite element analyses. The formation process of the self-locking structure. Preparation and characterization of electrodes. Plant electrophysiology testing and signal analysis. Stimulating and recording activities of the sciatic nerve in vivo and histology analysis. Regulation of the action of PI/PVA bilayers (PDF)

> Movie S1. Formation of a three-dimensional concatenated structure containing three helical segments (MP4)

> Movie S2. Formation of a bowknot shape (MP4)

> Movie S3. Formation of the self-locking structure (MP4)

> Movie S4. The process of mounting helical electrodes onto plant stems (MP4)

> Movie S5. Movement of the hindlimb during electrical stimulation using self-deforming electrodes (MP4)

> Movie S6. Composite nerve signals generated by mechanical stimulation of hindlimbs (MP4)

■ AUTHOR INFORMATION

Corresponding Authors

Changbo Liu − *School of Materials Science and Engineering, Beihang University, Beijing 100191, China; Key Laboratory of Intelligent Sensing Materials and Chip Integration Technology of Zhejiang Province, Hangzhou Innovation Institute of Beihang University, Hangzhou 310051, China;* orcid.org/0000-0003-1647-991X; Email: liuchb@buaa.edu.cn

Xing Sheng − *Department of Electronic Engineering, Beijing National Research Center for Information Science and Technology, Institute for Precision Medicine, Center for Flexible Electronics Technology, IDG/McGovern Institute for Brain Research, Tsinghua University, Beijing 100084, China;* orcid.org/0000-0002-8744-1700; Email: xingsheng@tsinghua.edu.cn

Yuan Deng − *Research Institute for Frontier Science, Beihang University, Beijing 100191, China; Key Laboratory of Intelligent Sensing Materials and Chip Integration Technology of Zhejiang Province, Hangzhou Innovation Institute of Beihang University, Hangzhou 310051, China;* orcid.org/0000-0002-1454-2965; Email: dengyuan@buaa.edu.cn

Authors

Yuanyuan Cui − *Research Institute for Frontier Science, Beihang University, Beijing 100191, China; Key Laboratory of Intelligent Sensing Materials and Chip Integration Technology of Zhejiang Province, Hangzhou Innovation Institute of Beihang University, Hangzhou 310051, China*

Lizhu Li − *Department of Electronic Engineering, Beijing National Research Center for Information Science and Technology, Institute for Precision Medicine, Center for Flexible Electronics Technology, IDG/McGovern Institute for Brain Research, Tsinghua University, Beijing 100084, China*

Yuqi Wang − *Department of Electronic Engineering, Beijing National Research Center for Information Science and Technology, Institute for Precision Medicine, Center for Flexible Electronics Technology, IDG/McGovern Institute for Brain Research, Tsinghua University, Beijing 100084, China*

Mengwei Sun − *School of Materials Science and Engineering, Beihang University, Beijing 100191, China*

Ben Jia − *School of Materials Science and Engineering, Beihang University, Beijing 100191, China*

Zhangming Shen − *Applied Mechanics Laboratory, Department of Engineering Mechanics and Laboratory of*

Flexible Electronics Technology, Tsinghua University, Beijing 100084, China

Complete contact information is available at:
https://pubs.acs.org/10.1021/acs.nanolett.3c03394

Author Contributions

Notes

The authors declare no competing financial interest.

■ ACKNOWLEDGMENTS

■ REFERENCES

(1) Kim, B. H.; Liu, F.; Yu, Y.; Jang, H.; Xie, Z.; Li, K.; Lee, J.; Jeong, J. Y.; Ryu, A.; Lee, Y.; Kim, D. H.; Wang, X.; Lee, K.; Lee, J. Y.; Won, S. M.; Oh, N.; Kim, J.; Kim, J. Y.; Jeong, S. J.; Jang, K. I.; Lee, S.; Huang, Y.; Zhang, Y.; Rogers, J. A. Mechanically Guided Post-Assembly of 3D Electronic Systems. *Adv. Funct. Mater.* **2018**, *28* (48), 1803149.

(2) Kim, H.; Gibson, J.; Maeng, J.; Saed, M. O.; Pimentel, K.; Rihani, R. T.; Pancrazio, J. J.; Georgakopoulos, S. V.; Ware, T. H. Responsive, 3D Electronics Enabled by Liquid Crystal Elastomer Substrates. *ACS Appl. Mater. Interfaces* **2019**, *11* (21), 19506–19513.

(3) Huang, Y.; Wu, H.; Xiao, L.; Duan, Y.; Zhu, H.; Bian, J.; Ye, D.; Yin, Z. Assembly and applications of 3D conformal electronics on curvilinear surfaces. *Materials Horizons* **2019**, *6* (4), 642–683.

(4) Wang, H.; Sun, P.; Yin, L.; Sheng, X. 3D electronic and photonic structures as active biological interfaces. *InfoMat* **2020**, *2* (3), 527–552.

(5) Zhao, Q.; Du, X. Multi-scale adaptions of dynamic bio-interfaces. *Smart Materials in Medicine* **2022**, *3*, 37–40.

(6) Sun, T.; Qing, G.; Su, B.; Jiang, L. Functional biointerface materials inspired from nature. *Chem. Soc. Rev.* **2011**, *40* (5), 2909–21.

(7) Xue, Z.; Jin, T.; Xu, S.; Bai, K.; He, Q.; Zhang, F.; Cheng, X.; Ji, Z.; Pang, W.; Shen, Z.; Song, H.; Shuai, Y.; Zhang, Y. Assembly of complex 3D structures and electronics on curved surfaces. *Sci. Adv.* **2022**, *8* (32), eabm6922.

(8) Zhao, Y.; Zhang, B.; Yao, B.; Qiu, Y.; Peng, Z.; Zhang, Y.; Alsaid, Y.; Frenkel, I.; Youssef, K.; Pei, Q.; He, X. Hierarchically Structured Stretchable Conductive Hydrogels for High-Performance Wearable Strain Sensors and Supercapacitors. *Matter* **2020**, *3* (4), 1196–1210.

(9) Yang, J. C.; Mun, J.; Kwon, S. Y.; Park, S.; Bao, Z.; Park, S. Electronic Skin: Recent Progress and Future Prospects for Skin-Attachable Devices for Health Monitoring, Robotics, and Prosthetics. *Adv. Mater.* **2019**, *31* (48), e1904765.

(10) Liu, Y.; Yang, T.; Zhang, Y.; Qu, G.; Wei, S.; Liu, Z.; Kong, T. Ultrastretchable and Wireless Bioelectronics Based on All-Hydrogel Microfluidics. *Adv. Mater.* **2019**, *31* (39), e1902783.

(11) Li, J.; Wasley, T.; Nguyen, T. T.; Ta, V. D.; Shephard, J. D.; Stringer, J.; Smith, P.; Esenturk, E.; Connaughton, C.; Kay, R. Hybrid additive manufacturing of 3D electronic systems. *Journal of Micromechanics and Microengineering* **2016**, *26* (10), 105005.

(12) Le Borgne, B.; Liu, S.; Morvan, X.; Crand, S.; Sporea, R. A.; Lu, N.; Harnois, M. Water Transfer Printing Enhanced by Water-Induced Pattern Expansion: Toward Large-Area 3D Electronics. *Advanced Materials Technologies* **2019**, *4* (4), 1800600.

(13) Sandstrom, A.; Asadpoordarvish, A.; Enevold, J.; Edman, L. Spraying light: ambient-air fabrication of large-area emissive devices on complex-shaped surfaces. *Adv. Mater.* **2014**, *26* (29), 4975–80.

(14) Sakai, M.; Watanabe, K.; Ishimine, H.; Okada, Y.; Yamauchi, H.; Sadamitsu, Y.; Kudo, K. Thermal Molding of Organic Thin-Film Transistor Arrays on Curved Surfaces. *Nanoscale Res. Lett.* **2017**, *12* (1), 349.

(15) Tan, H. W.; Choong, Y. Y. C.; Kuo, C. N.; Low, H. Y.; Chua, C. K. 3D printed electronics: Processes, materials and future trends. *Prog. Mater. Sci.* **2022**, *127*, 100945.

(16) Ware, T.; Simon, D.; Hearon, K.; Liu, C.; Shah, S.; Reeder, J.; Khodaparast, N.; Kilgard, M. P.; Maitland, D. J.; Rennaker, R. L., 2nd; Voit, W. E. Three-Dimensional Flexible Electronics Enabled by Shape Memory Polymer Substrates for Responsive Neural Interfaces. *Macromol. Mater. Eng.* **2012**, *297* (12), 1193–1202.

(17) Reeder, J.; Kaltenbrunner, M.; Ware, T.; Arreaga-Salas, D.; Avendano-Bolivar, A.; Yokota, T.; Inoue, Y.; Sekino, M.; Voit, W.; Sekitani, T.; Someya, T. Mechanically adaptive organic transistors for implantable electronics. *Adv. Mater.* **2014**, *26* (29), 4967–73.

(18) Wang, H.; Wang, Y.; Tee, B. C.; Kim, K.; Lopez, J.; Cai, W.; Bao, Z. Shape-Controlled, Self-Wrapped Carbon Nanotube 3D Electronics. *Adv. Sci. (Weinh)* **2015**, *2* (9), 1500103.

(19) Zhang, Y.; Zheng, N.; Cao, Y.; Wang, F.; Wang, P.; Ma, Y.; Lu, B.; Hou, G.; Fang, Z.; Liang, Z.; Yue, M.; Li, Y.; Chen, Y.; Fu, J.; Wu, J.; Xie, T.; Feng, X. Climbing-inspired twining electrodes using shape memory for peripheral nerve stimulation and recording. *Sci. Adv.* **2019**, *5* (4), eaaw1066.

(20) Zhao, Q.; Wang, J.; Cui, H.; Chen, H.; Wang, Y.; Du, X. Programmed Shape-Morphing Scaffolds Enabling Facile 3D Endothelialization. *Adv. Funct. Mater.* **2018**, *28* (29), 1801027.

(21) Woodington, B. J.; Curto, V. F.; Yu, Y.-L.; Martínez-Domínguez, H.; Coles, L.; Malliaras, G. G.; Proctor, C. M.; Barone, D. G. Electronics with shape actuation for minimally invasive spinal cord stimulation. *Sci. Adv.* **2021**, *7* (26), eabg7833.

(22) Hiendlmeier, L.; Zurita, F.; Vogel, J.; Del Duca, F.; Al Boustani, G.; Peng, H.; Kopic, I.; Nikic, M.; T, F. T.; Wolfrum, B. 4D-Printed Soft and Stretchable Self-Folding Cuff Electrodes for Small-Nerve Interfacing. *Adv. Mater.* **2023**, *35* (12), e2210206.

(23) Hao, X. P.; Li, C. Y.; Zhang, C. W.; Du, M.; Ying, Z.; Zheng, Q.; Wu, Z. L. Self-Shaping Soft Electronics Based on Patterned Hydrogel with Stencil-Printed Liquid Metal. *Adv. Funct. Mater.* **2021**, *31* (47), 2105481.

(24) Karnaushenko, D.; Munzenrieder, N.; Karnaushenko, D. D.; Koch, B.; Meyer, A. K.; Baunack, S.; Petti, L.; Troster, G.; Makarov, D.; Schmidt, O. G. Biomimetic Microelectronics for Regenerative Neuronal Cuff Implants. *Adv. Mater.* **2015**, *27* (43), 6797–805.

(25) Abedalwafa, M.; Wang, F. J.; Wang, L.; Li, C. J. Biodegradable Poly-Epsilon-Caprolactone (Pcl) For Tissue Engineering Applications: A Review. *Rev. Adv. Mater. Sci.* **2013**, *34* (2), 123–140.

(26) Pitt, C. G.; Chasalow, F. I.; Hibionada, Y. M.; Klimas, D. M.; Schindler, A. Aliphatic polyesters. I. The degradation of poly(ϵ-caprolactone) in vivo. *Journal of Applied Polymer Science* **1981**, *26* (11), 3779–3787.

(27) Chiellini, E.; Corti, A.; D'Antone, S.; Solaro, R. Biodegradation of poly (vinyl alcohol) based materials. *Prog. Polym. Sci.* **2003**, *28* (6), 963–1014.

(28) Ullah, K.; Sohail, M.; Murtaza, G.; Khan, S. A. Natural and synthetic materials based CMCh/PVA hydrogels for oxaliplatin

delivery: Fabrication, characterization, In-Vitro and In-Vivo safety profiling. *Int. J. Biol. Macromol.* **2019**, *122*, 538−548.

(29) Rajaram, K.; Yang, S. M.; Hwang, S.-W. Transient, Biodegradable Energy Systems as a Promising Power Solution for Ecofriendly and Implantable Electronics. *Advanced Energy and Sustainability Research* **2022**, *3* (9), 2100223.

(30) Gautam, S.; Dinda, A. K.; Mishra, N. C. Fabrication and characterization of PCL/gelatin composite nanofibrous scaffold for tissue engineering applications by electrospinning method. *Mater. Sci. Eng. C Mater. Biol. Appl.* **2013**, *33* (3), 1228−35.

(31) Zhang, Y.; Ouyang, H.; Lim, C. T.; Ramakrishna, S.; Huang, Z. M. Electrospinning of gelatin fibers and gelatin/PCL composite fibrous scaffolds. *J. Biomed Mater. Res. B Appl. Biomater* **2005**, *72* (1), 156−65.

(32) Zhao, Z.; Kuang, X.; Yuan, C.; Qi, H. J.; Fang, D. Hydrophilic/Hydrophobic Composite Shape-Shifting Structures. *ACS Appl. Mater. Interfaces* **2018**, *10* (23), 19932−19939.

(33) Palleau, E.; Morales, D.; Dickey, M. D.; Velev, O. D. Reversible patterning and actuation of hydrogels by electrically assisted ionoprinting. *Nat. Commun.* **2013**, *4*, 2257.

(34) Jackson, S. D.; Mittal, R. O. Automatic generation of 2-axis laser-cutter NC machine program and path planning from CAD. *Computers in Industry* **1993**, *21* (2), 223−231.

(35) Genc, S.; Messler, R. W.; Gabriele, G. A. A systematic approach to integral snap-fit attachment design. *Research in Engineering Design* **1998**, *10* (2), 84−93.

(36) Klahn, C.; Singer, D.; Meboldt, M. Design Guidelines for Additive Manufactured Snap-Fit Joints. *Procedia CIRP* **2016**, *50*, 264−269.

(37) Suri, G.; Luscher, A. F. Structural Abstraction in Snap-fit Analysis. *Journal of Mechanical Design* **2000**, *122* (4), 395−402.

(38) Stavrinidou, E.; Gabrielsson, R.; Gomez, E.; Crispin, X.; Nilsson, O.; Simon, D. T.; Berggren, M. Electronic plants. *Science advances* **2015**, *1* (10), e1501136.

(39) Fromm, J.; Lautner, S. Electrical signals and their physiological significance in plants. *Plant Cell Environ* **2007**, *30* (3), 249−257.

(40) Kim, J. J.; Allison, L. K.; Andrew, T. L. Vapor-printed polymer electrodes for long-term, on-demand health monitoring. *Science Advances* **2019**, *5* (3), eaaw0463.

(41) Li, J. H.; Fan, L. F.; Zhao, D. J.; Zhou, Q.; Yao, J. P.; Wang, Z. Y.; Huang, L. Plant electrical signals: A multidisciplinary challenge. *J. Plant Physiol* **2021**, *261*, 153418.

(42) Volkov, A. G. *Plant Electrophysiology: Signaling and Responses*; Springer: Berlin Heidelberg, 2012.

(43) Lacour, S. P.; Courtine, G.; Guck, J. Materials and technologies for soft implantable neuroprostheses. *Nat. Rev. Mater.* **2016**, *1* (10), 1−14.

(44) Boon, P.; Vonck, K.; Reuck, J. D.; Caemaert, J. Vagus nerve stimulation for refractory epilepsy. *Seizure* **2001**, *10* (6), 448−455.

(45) Famm, K.; Litt, B.; Tracey, K. J.; Boyden, E. S.; Slaoui, M. A jump-start for electroceuticals. *Nature* **2013**, *496* (7444), 159−161.

(46) Graczyk, E. L.; Resnik, L.; Schiefer, M. A.; Schmitt, M. S.; Tyler, D. J. Home Use of a Neural-connected Sensory Prosthesis Provides the Functional and Psychosocial Experience of Having a Hand Again. *Sci. Rep* **2018**, *8* (1), 9866.

(47) Grill, W. M.; Kirsch, R. F. Neuroprosthetic applications of electrical stimulation. *Assist Technol.* **2000**, *12* (1), 6−20.

(48) Ramos-Remus, C.; Duran-Barragan, S.; Castillo-Ortiz, J. D. Beyond the joints: neurological involvement in rheumatoid arthritis. *Clin Rheumatol* **2012**, *31* (1), 1−12.

(49) Sinkjaer, T.; Haugland, M.; Inmann, A.; Hansen, M.; Nielsen, K. D. Biopotentials as command and feedback signals in functional electrical stimulation systems. *Medical Engineering & Physics* **2003**, *25* (1), 29−40.

(50) Xiang, Z.; Yen, S. C.; Sheshadri, S.; Wang, J.; Lee, S.; Liu, Y. H.; Liao, L. D.; Thakor, N. V.; Lee, C. Progress of Flexible Electronics in Neural Interfacing - A Self-Adaptive Non-Invasive Neural Ribbon Electrode for Small Nerves Recording. *Adv. Mater.* **2016**, *28* (22), 4472−9.

(51) Decataldo, F.; Cramer, T.; Martelli, D.; Gualandi, I.; Korim, W. S.; Yao, S. T.; Tessarolo, M.; Murgia, M.; Scavetta, E.; Amici, R.; Fraboni, B. Stretchable Low Impedance Electrodes for Bioelectronic Recording from Small Peripheral Nerves. *Sci. Rep* **2019**, *9* (1), 10598.

(52) Delianides, C.; Tyler, D.; Pinault, G.; Ansari, R.; Triolo, R. Implanted High Density Cuff Electrodes Functionally Activate Human Tibial and Peroneal Motor Units Without Chronic Detriment to Peripheral Nerve Health. *Neuromodulation* **2020**, *23* (6), 754−762.

(53) Lee, S.; Peh, W. Y. X.; Ho, J. S.; Thakor, N. V.; Yen, S. C.; Lee, C. In Batteryless Pelvic Nerve Direct Modulation for Bladder Voding Using an Active Neural Clip, *2018 IEEE 13th Annual International Conference on Nano/Micro Engineered and Molecular Systems (NEMS), 22−26 April 2018*; 2018; pp 452−455.

(54) Ong, X. C.; Huang, W. C.; Kwon, I. S.; Gopinath, C.; Wu, H.; Fisher, L. E.; Gaunt, R. A.; Bettinger, C. J.; Fedder, G. K. In Ultra-compliant peripheral nerve cuff electrode with hydrogel adhesion, *2018 IEEE Micro Electro Mechanical Systems (MEMS), 21−25 Jan. 2018*; 2018; pp 376−379.

(55) Tyler, D. J.; Durand, D. M. Functionally selective peripheral nerve stimulation with a flat interface nerve electrode. *IEEE Trans Neural Syst. Rehabil Eng.* **2002**, *10* (4), 294−303.

(56) Heo, D. N.; Kim, H. J.; Lee, Y. J.; Heo, M.; Lee, S. J.; Lee, D.; Do, S. H.; Lee, S. H.; Kwon, I. K. Flexible and Highly Biocompatible Nanofiber-Based Electrodes for Neural Surface Interfacing. *ACS Nano* **2017**, *11* (3), 2961−2971.

(57) Lee, S.; Sheshadri, S.; Xiang, Z.; Delgado-Martinez, I.; Xue, N.; Sun, T.; Thakor, N. V.; Yen, S.-C.; Lee, C. Selective stimulation and neural recording on peripheral nerves using flexible split ring electrodes. *Sens. Actuators, B* **2017**, *242*, 1165−1170.

(58) Song, K. I.; Seo, H.; Seong, D.; Kim, S.; Yu, K. J.; Kim, Y. C.; Kim, J.; Kwon, S. J.; Han, H. S.; Youn, I.; Lee, H.; Son, D. Adaptive self-healing electronic epineurium for chronic bidirectional neural interfaces. *Nat. Commun.* **2020**, *11* (1), 4195.

Supporting Information

Water-Responsive 3D Electronics for Smart Biological Interfaces

Yuanyuan Cui,[1,4]† Lizhu Li,[2]† Changbo Liu,[3,4]* Yuqi Wang,[2] Mengwei Sun,[3] Ben Jia,[3] Zhangming Shen,[5,6] Xing Sheng,[2]* Yuan Deng,[1,4]*

[1] Research Institute for Frontier Science, Beihang University, Beijing 100191, China.

[2] Department of Electronic Engineering, Beijing National Research Center for Information Science and Technology, Institute for Precision Medicine, Center for Flexible Electronics Technology, IDG/McGovern Institute for Brain Research, Tsinghua University, Beijing 100084, China.

[3] School of Materials Science and Engineering, Beihang University, Beijing 100191, China.

[4] Key Laboratory of Intelligent Sensing Materials and Chip Integration Technology of Zhejiang Province, Hangzhou Innovation Institute of Beihang University, Hangzhou 310051, China.

[5] Applied Mechanics Laboratory, Department of Engineering Mechanics, Tsinghua University, Beijing 100084, China.

[6] Laboratory of Flexible Electronics Technology, Tsinghua University, Beijing 100084, China.

Note S1. Preparation of films.

Before the film casting, the glass sheet is cleaned with ethyl alcohol and deionized (DI) water, followed by heating and drying at 80°C for 20 min. PCL (average molecular weight of ~80,000; Macklin reagent) solution (20 wt % in N, N-Dimethylformamide) is spin-cast onto the glass sheet and then dried at 80°C for 5min to get thin PCL film. Thick polyurethane tape is used to form a mold around the glass sheet. The surface of the PCL layer is treated with vacuum plasma to increase the hydroxyl content on the surface to make the surface hydrophilic. And then a given mass of 10% PVA (average molecular weight of ~80,000; alcoholysis degree of 88%; Macklin reagent) aqueous solution is poured on the PCL film and dried at 80°C for 2 hours.

Note S2. Characterization of PVA, PCL and PVA/PCL bilayers.

The UV-Vis-IR absorption spectra of the PVA xerogels is characterized by using a spectrophotometer (Figure S3a).

Stress-strain curves of the polymer films are characterized by an electronic tensile testing machine and then calculated Young's modulus (Figure S3b). To test Young's modulus of PVA and PCL film, samples made into strips with a length of 10 cm and a width of 5 cm are stretched at a constant rate on a tensile testing machine to obtain a load-displacement curve. Then the stress-strain curve is calculated based on the size of the sample. As shown in Figure S3b, the elastic modulus of the sample is calculated from the elastic portion of the stress-strain curve. The test results show that the elastic modulus of PVA dry gel film is about 200MPa, and that of PCL film is about 100MPa.

To test the swelling behaviors of PVA, samples made of a rectangular parallelepiped with a side length of 2mm and a height of 200 μm are immersed in water. A grid pattern is set under the sample for convenient size calculation. An industrial microscope is used to catch photos

during the swelling process. Figure S1a and Figure S1b show the swelling kinetics of PVA. The linear swelling ratio is calculated through the following equation:

$$\alpha = \frac{L_{swelling} - L_{dry}}{L_{dry}}$$

Here, L dry is the initial side length of the cuboid, and L swelling is the side length after swelling. Figure S1c and Figure S1d show the swelling of PVA film in three directions. The PVA film prepared has an isotropic linear swelling rate of about 0.7, which is used for subsequent model calculations.

Hydrophilicity of the PCL film is measured with the use of a video contact angle instrument (Figure S2a). Deionized water (2 µL) was automatically dropped onto the flat PCL film. The contact angles indicating the wetting ability of the materials were calculated automatically. The measured water contact angle of the PCL film is 102.6°, demonstrating its hydrophobicity. To demonstrate that the PCL hardly absorbs water and swells, samples made of a rectangular parallelepiped with a side length of 2 mm and a height of 200 µm are immersed in water (Figure S2b). A grid pattern is set under the sample for convenient size calculation. An industrial microscope is used to catch photos during the process. After 200 minutes of immersion, there is no significant size change in the PCL film, demonstrating that PCL does not experience water absorption and expansion.

Note S3. Laser processing.

The surface of the PVA layer is scribed by laser. At the same time, the contour of the initial two-dimensional shape is also cut by laser to obtain the designed sample. Laser processing is carried out using a femtosecond laser (Light Conversion PHAROS-20). The laser wavelength is 343nm. Laser scanning speed is 100 mm/s. The shape of a single trench is a V-groove (Figure S4). By adjusting the average power of the laser, the size of laser damage spots on PVA can be

changed, resulting in trenches with different opening widths. When the average laser power is 2W, the width of the single trench is about 5 μm (Figure S4a). When the average laser power is 5W, the width of a single trench is about 15 μm (Figure S4c). When the average laser power is 8w, the width of a single trench is about 25 μm (Figure S4e). When the average laser power is 16w, the width of a single trench is about 80 μm (Figure S4b). At the same time, the depth of a single trench also increases with the increase of the average laser power. When the average laser power remains constant, increasing the number of scans is used to increase the depth of the trench. When the average laser power is 5W and the number of scans is 7, the trench depth is about 150 μm (Figure S4d). Approximate rectangular trenches appear with multiple adjacent trenches. When the average laser power is 8W and the number of scans is 5, by processing four adjacent trenches with a center spacing of 25 μm, a rectangular trench with a width of about 100 μm and a depth of about 130 μm can be obtained (Figure S4f). The pre-designed laser processing patterns (CAD data) and parameters are input into the laser control system, and the controller automatically completes scribing at one time.

Note S4. Modeling the bilayer mismatched expansion structure.

Mechanical modeling of double-layer deformation caused by mismatched expansion has been an intensive research in the past. The classical thermal expansion and bending equation of double-layer metal beams was proposed in 1925[1]:

$$\frac{1}{\rho} = \frac{6(\alpha_2 - \alpha_1)(t - t_0)(1 + m)^2}{h(3(1 + m)^2 + (1 + mn)\left(m^2 + \frac{1}{mn}\right))} \qquad (1)$$

here, ρ Is the final bending curvature, α_1 and α_2 is the thermal expansion coefficient of the passive layer and the active layer, t_0 and t are the initial and heating temperatures, respectively, m is the ratio of the thickness of the passive layer to the thickness of the active layer, h is the total thickness of the structure, and n is the ratio of the elastic modulus of the

4

passive layer to the elastic modulus of the active layer. This bimetallic beam thermal expansion model is also applied as a classical equation to the swelling deformation model. It is the simplest model for complex processes, achieving qualitative and semi quantitative prediction of strain mismatch two-layer deformation structure-function relationships. However, the classical equation and most of the previous analytical solutions for swelling bilayer only considered the deformation of the double-layer structure at equilibrium swelling ratio, where the time history of the actuation was not considered[2-4], that is, the diffusion process of solvents during swelling induced deformation, the spatiotemporal distribution of solvents, and the change in modulus caused by changes in the water content of the actuating layer. On the other hand, the classical equation is more suitable for small deformation of the double-layer beam due to the use of parameters such as the bending stiffness of the beam, and has low prediction accuracy in two-layer swelling deformation structures. Continuum frameworks were proposed to describe the coupling between diffusion and large deformation in polymer hydrogels[5]. Then the theories were utilized to obtain transient behaviors of swelling hydrogels and water-driven devices by finite element method (FEM)[6-9]. However, it is computationally inefficient in solving the coupling for complex structures, with extremely small time steps and dense meshes are utilized to ensure convergence. A simple model for the hydrophilic/hydrophobic bilayer deformation was developed, in which the diffusion of water was described by the one-dimensional diffusion equation and transient deformation during swelling can be captured[10]. When the swelling reaches equilibrium, the curvature of the bilayer structure is obtained as

$$\kappa = \frac{\frac{1}{2}E_a ln\lambda^e[(E_a h^2 - E_p H^2)h - (E_a h + E_p H)h^2]}{\frac{1}{4}(E_a h^2 - E_p H^2)^2 - \frac{1}{3}(E_a h^3 + E_p H^3)(E_a h + E_p H)} \qquad (2)$$

5

here, κ is curvature, E_a and E_p are Young's modulus of actuation layer and passive layer, λ^e is the equilibrium swelling ratio, h and H are thickness of actuation layer and passive layer. Our model is based on this model and incorporates the impact of laser scribing trenches.

The bending curvature of the whole shape-shifting bilayer is divided into two parts (laser scribing part and unscribed part) for calculation. The curvature generated by the unscribed part which is defined as A is divided into a rapidly expanding layer ($(a_2 - a_3)$ part) in Figure S5) and a subsequent expansion layer (a_3 part in Figure S5) to calculate using eqs (2).

Due to the reduction of the section moment of inertia at the scribing trenches site, the bending stiffness will decrease, and the bending will preferentially follow the direction of trench arrangement. When the effect of laser scribing trenches on the curvature is considered, it is believed that besides bending, folding phenomenon also occurs at the scribing parts. The curvature generated by bending (defined as C) is still calculated by eqs (2). Schematic diagram of bending model of bilayer structure with a laser scribing trench is shown in Figure S5. Figure S5a and Figure S5b show before and after swelling, respectively. The angle of the fold is obtained by equalizing the force produced by compressing swollen gel at both sides of the scribed part with the force required to squeeze the gel on the inside of the fold. The force produced by compressing swollen gel at both sides of the scribed part can be expressed as

$$F = \varepsilon E_3 (a_2 - a_3)(1 + D)b \qquad (3)$$

here, E_3 is Young's modulus of PVA gel after water swelling, ε is compressive strain of swollen gel at both sides of the scribed part, a_1 is the thickness of the PCL film, a_2 is the thickness of the PVA film, a_3 is remaining PVA thickness at the scribing trench, D is the linear expansion rate of the PVA, which is numerically equal to $\lambda^e - 1$ in the eqs (2), b is

the width of the bilayer. The force required to squeeze the gel on the inside of the fold can be expressed as

$$F = \int_0^{\frac{a_3}{\cos\alpha}} \frac{h\tan\alpha}{\frac{h}{\tan\alpha}} E_2 b \, dh + \int_0^{\frac{a_1}{\cos\alpha}} \frac{(h + \frac{a_3}{\cos\alpha})\tan\alpha}{h + \frac{a_3}{\cos\alpha}} E_1 b \, dh \qquad (4)$$

here, E_1 and E_2 are Young's modulus of PCL layer and PVA layer, α is half of the folded corner. Combining eqs (3) and (4),

$$\frac{\tan^2\alpha}{\cos\alpha} = \frac{\varepsilon E_3(a_2 - a_3)(1 + D)}{E_2 a_3 + E_1 a_1} \qquad (5)$$

Then the curvature of the whole bilayer can be expressed as

$$y = \frac{\left(L - w\left(\frac{L}{x} - 1\right)\right)A + \left(\frac{L}{x} - 1\right)B + w\left(\frac{L}{x} - 1\right)C}{L} \qquad (6)$$

here, L is the total length of the bilayer film. w is the groove width of the trench. x is the arrangement line spacing of scribing trenches. A refers to the curvature generated by the unscribed part, which is divided into a rapidly expanding layer (($a_2 - a_3$) part) and a subsequent expansion layer (a_3 part) to calculate. C is the curvature generated by the remaining PVA at the scribed part. A and C are directly calculated by eqs (2), and B is the folding angle at the scribing trench, which is 2α calculated by eqs (5). Table S2 shows the parameter values used in the equation.

When using the same parameters as in the experiment (the total length of the bilayer is 3 mm, the PVA thickness is 180 μm, the PCL thickness is 70 μm, the depth of trench is 100 μm, the width of trench is 30 μm), the calculated A is 0.5635, B is 0.08486, C is 0.2473. The curvature of the whole bilayer can be expressed as

$$y = \frac{\left(3 - 0.03\left(\frac{3}{x} - 1\right)\right)0.5635 + \left(\frac{3}{x} - 1\right)0.08486 + 0.03\left(\frac{3}{x} - 1\right)0.2473}{3} \qquad (7)$$

The experimental results are in good agreement with the model prediction results (Figure 1f).

Note S5. Dependence of curvature and actuation time on width of trenches and depth of trenches.

Different curvatures and actuation times are obtained on films with the same thickness composition by adjusting the width of trenches and depth of trenches. (Figure 1g and 1h). For the experiment on the influence of width of trenches, a series of samples with the same dimension (3 mm * 3 mm) and thickness composition (PVA 180 μm, PCL 70 μm) are scribed with laser-induced trenches which have the same depth (100 μm), arrangement line spacing (0.3 mm), and different width of 30 μm-150 μm. As the width of trenches increases from 30 μm to 150 μm, the curvature of the bilayer curling action gradually decreases from 0.784 mm^{-1} to 0.513 mm^{-1} (orange symbols in Figure 1g), and the actuation time of the bilayer decreases from 374 s to 217 s (blue symbols in Figure 1g). For the experiment on the influence of depth of trenches, a series of samples with the same dimension (3 mm * 3 mm) and thickness composition (PVA 180 μm, PCL 70 μm) are scribed with laser-induced trenches which have the same width (60 μm), arrangement line spacing (0.3 mm), and different depth of 15 μm-170 μm. As the depth of trenches increases from 15 μm to 170 μm, the curvature of the bilayer curling action gradually increases from 0.602 mm^{-1} to 0.658 mm^{-1} (orange symbols in Figure 1h), and the actuation time of the bilayer decreases from 393 s to 297 s (blue symbols in Figure 1h).

An example is provided to illustrate the independent control of actuation time (Figure S6). By simultaneously adjusting the line spacing and trench width, two bilayers with the same

curvature and different actuation time can be obtained. As shown in Figure S6, two bilayer samples have the same dimension (3 mm * 3 mm) and thickness composition (PVA 180 μm, PCL 70 μm) are scribed with laser-induced trenches which have the same depth (100 μm), different arrangement line spacing (Sample 1: 0.3 mm, Sample 2: 0.6 mm), and different width (Sample 1:50 μm, Sample 2: 30 μm). These two bilayer samples have the same curvature of 0.67mm^{-1} and a 51 s difference in actuation time.

Note S6. Finite element analyses.

Based on elasticity theory and stationarity principles, we have established a finite element analysis (FEA) simulation model. Finite element stimulations (Abaqus) are used to analyze the deformation process of bilayers with different scribing trenches patterns. The color of the nephogram shows the stress of the structure at this point. In the simulation, a model with a size of 1:1 to the actual sample is used, and thermal expansion is used instead of water absorption expansion to qualitatively analyze the deformation. The product of the set linear thermal expansion coefficient and the temperature difference is equal to the actual linear swelling rate of the sample. The elastic modulus of PVA was set to decrease linearly with the increase of thermal field temperature to better simulate the deformation process.

Note S7. The formation process of the self-locking structure.

The detailed illustrations for components of the self-locking structure are shown in Figure S7a. The formation process of the self-locking structure: When exposed to humidity, The "receptacle part" on one side (the green part in the figure) will first bend up, and the two "protrusion part" on the other side (the blue part in the figure) will also bend inward. Then, with the bending of the entire rectangular structure, the "protrusion part" will be pushed into the back of the "receptacle part" and be stuck so that the entire structure finishes with self-locking (Movie S3). The precise cooperation of deformation in different parts of the bilayer in both temporal and

9

spatial dimensions is the key to the successful assembly self-locking structure. When the action of the "receptacle part" is not fast enough and bends with the same actuation time as the entire rectangular structure, the "protrusion part" will not be able to be pushed into the back of the "receptacle part", but will bend at the front of the "receptacle part" (Movie S3 and Figure S7b).

Note S8. Preparation of spiral twining electrophysiological monitoring electrode and self-rolling nerve electrode.

After obtaining the substrate through laser processing and scribing trenches, layers of 10-nm Ni and 100-nm Au are deposited onto the surface of the PCL film using Magnetron sputtering, and the deposition rate of the metal layer was controlled at ~0.33 nm/s. The patterning of metal was achieved through a pre-designed mask (Figure S10).

Note S9. Characterization of the metal nanofilm and the interface between the metal nanofilm and PCL before and after bilayer bending.

Bilayers with metal nanofilm are observed under optical microscopy and scanning electron microscopy before and after bending (Figure S11). The results showed that the gold nanofilm showed wrinkles after bilayer bending, but no obvious cracks appeared, indicating that the gold nanofilm can maintain good conductivity during the 3D assembly process. Before and after the bilayer bending, there is no obvious delamination problem at the interface between the gold nanofilm and PCL.

Note S10. Preparation of agar-based electrode.

The preparation of agar viscous solution followed the protocol by Mousavi et al.[11] Agar powder was weighted and added in 10 mM KCl at 0.5% (w/v). The mixture was heated to boil and kept boiling for 10 min before cooling to room temperature with magnetic stirring at 300 rpm. The resultant mixture is a viscous translucent liquid. Cut a 4-cm-long piece of silver wire, and then

bend one end by 180° to obtain a half-circle with a diameter of ~1 mm. Chloridize the curved end of the wire on 1–2 cm to coat it with a layer of AgCl. After a few uses, the wires need to be rechloridized.

Note S11. Plant electrophysiology testing.

Wound-induced potential changes and action potential caused by non-noxious stimulation in Anthurium andraeanum, were recorded using spiral twining electrodes and inserted metal wires. In addition, the noise signal caused by mechanical disturbance is evaluated in the test of the twining electrode and agar-based electrode. Anthurium andraeanum was purchased from a local market. On the day before testing, plants were watered and left undisturbed in a room maintained at 24-25°C and 50-60% humidity.

For testing using spiral twining electrodes, the deformable electrode in flat state was put into the water and was taken out after 10-20s. Then it was put on the plant stem to autonomously deformed and wrapped on the stem. For invasive testing, chlorinated Ag wires were inserted in stems at about 2 mm depth, and plants need to be undisturbed for at least two hours before testing to recover from the potential signal of inserted injury. To assemble the agar-wire electrodes, an Ag wire with a bent tip was firstly chlorinated and then held in place by an electrode manipulator. Agar viscous solution was then slowly dropped at the plant interface carefully with the bent tip of the ager-wire being wrapped in. Ag/AgCl reference electrode was inserted in moist soil setting the reference potential.

Flame wounding on Anthurium andraeanum followed methods reported previously.[12] The flame from a lighter was placed underneath a leaf tip for 3s. Before wounding, the leaf to be wounded was stabilized to minimize leaf movements during wounding. Signals from helical electrodes and control electrodes were collected simultaneously at a sampling frequency of 50 Hz by data acquisition systems.

11

Note S12. Electrophysiology signal analysis.

The amplitude of variation potential signal is calculated as the difference between the lowest point of potential after fire injury and the baseline of potential before injury, that is, the depolarization amplitude. The amplitude of action potential is calculated as the difference between the highest peak potential and the lowest peak potential.

Signal-to-noise ratio (SNR) was calculated through

$$SNR = 10lg\frac{P_s}{P_n}$$

where P_s is the mean value of the square of the amplitude of a group of signals in one test, and P_n is mean square background noise amplitude.

Note S13. Animal care.

For stimulating and recording activities of the sciatic nerve in vivo, all animal protocols used were in accordance with the institutional guidelines of Tsinghua University and were proved by Institutional Animal Care and Use Committee (IACUC). All animals are socially housed in a 12 h/12 h (lights on at 8 am) light/dark cycle, with access to food pellets and water ad libitum.

For biocompatibility test and histology analysis, all animal work was approved by Wuhan Servicebio Technology Co., Ltd., China, and the ethical approval protocol number was Servicebio Animal Welfare NO. 2022158.

Note S14. Stimulating and recording activities of the sciatic nerve in vivo.

Rat (SD, 6 weeks old) was purchased from VitalRiver (Beijing, China). Animals were anesthetized with an intraperitoneal injection of 1% pentobarbital sodium anesthetic (60 mg/kg) before surgery and then fixed on the operating table. Using a scalpel and surgical nickel, the sciatic nerve was exposed without muscle damage by being isolated from surrounding

connective tissue. The shape-shifting bilayers were put under the nerve and given PBS to make it curl around the sciatic nerve to give it a good attachment to the nerve. The stimulation signal with a frequency of 0.5 Hz, a pulse current of 0.08 mA to 0.2 mA, and a pulse width of 0.2 ms was achieved through a multi-channel electrophysiological acquisition and processing system (Chengdu Instrument Factory, RM6240E/EC). A recording electrode was inserted into the tibial related-muscle region, collecting electromyography (EMG) signals with a sampling rate of 20 kHz and a low-pass filter at 300 Hz. During the recording experiment, we continuously give increased physical stimulation to the soles of rat by surgical tweezers, while the sciatic nerve signals were collected by the deformed bilayers connected to RM6240E/EC with a sampling rate of 20 kHz and a low-pass filter at 300 Hz. A camera captured the hindlimb lifting with a sampling rate of 30 frames/s.

Note S15. Histology analysis.

For histological imaging, sciatic nerves of rats with and without implants were extracted (~5 mm length) and fixed with 4% paraformaldehyde in PBS overnight. Subsequently, standard methods of embedding, slicing, and hematoxylin-eosin (H&E) staining were imposed. The images were monitored using an optical microscope.

Note S16. Regulation of the action of PI/PVA bilayers.

The commonly used bioelectronic materials polyimide is used as the passive layer to demonstrate its feasibility in bilayer structures and the scalability of the strategy. In the PI/PVA bilayer structure, laser scribing trenches can also precisely regulate the action of the bilayer (Figure S9).

References

1. Timoshenko, S., Analysis of Bi-Metal Thermostats. *J. Opt. Soc. Am.* **1925,** *11* (3), 233-255.
2. Abdolahi, J.; Baghani, M.; Arbabi, N.; Mazaheri, H., Analytical and numerical analysis of swelling-induced large bending of thermally-activated hydrogel bilayers. *International Journal of Solids and Structures* **2016,** *99*, 1-11.
3. Drozdov, A. D.; Christiansen, J. d., Swelling-induced bending of bilayer gel beams. *Composite Structures* **2016,** *153*, 961-971.
4. Nardinocchi, P.; Puntel, E., Finite bending solutions for layered gel beams. *International Journal of Solids and Structures* **2016,** *90*, 228-235.
5. Chester, S. A.; Anand, L., A coupled theory of fluid permeation and large deformations for elastomeric materials. *Journal of the Mechanics and Physics of Solids* **2010,** *58* (11), 1879-1906.
6. An, N.; Li, M.; Zhou, J., Predicting origami-inspired programmable self-folding of hydrogel trilayers. *Smart Materials and Structures* **2016,** *25* (11).
7. Chester, S. A.; Di Leo, C. V.; Anand, L., A finite element implementation of a coupled diffusion-deformation theory for elastomeric gels. *International Journal of Solids and Structures* **2015,** *52*, 1-18.
8. Duan, Z.; Zhang, J.; An, Y.; Jiang, H., Simulation of the Transient Behavior of Gels Based on an Analogy Between Diffusion and Heat Transfer. *Journal of Applied Mechanics* **2013,** *80* (4).
9. Guo, W.; Li, M.; Zhou, J., Modeling programmable deformation of self-folding all-polymer structures with temperature-sensitive hydrogels. *Smart Materials and Structures* **2013,** *22* (11).
10. Zhao, Z.; Kuang, X.; Yuan, C.; Qi, H. J.; Fang, D., Hydrophilic/Hydrophobic Composite Shape-Shifting Structures. *ACS Appl Mater Interfaces* **2018,** *10* (23), 19932-19939.
11. Mousavi, S. A.; Nguyen, C. T.; Farmer, E. E.; Kellenberger, S., Measuring surface potential changes on leaves. *Nat Protoc* **2014,** *9* (8), 1997-2004.
12. Luo, Y.; Li, W.; Lin, Q.; Zhang, F.; He, K.; Yang, D.; Loh, X. J.; Chen, X., A Morphable Ionic Electrode Based on Thermogel for Non-Invasive Hairy Plant Electrophysiology. *Adv Mater* **2021,** *33* (14), e2007848.
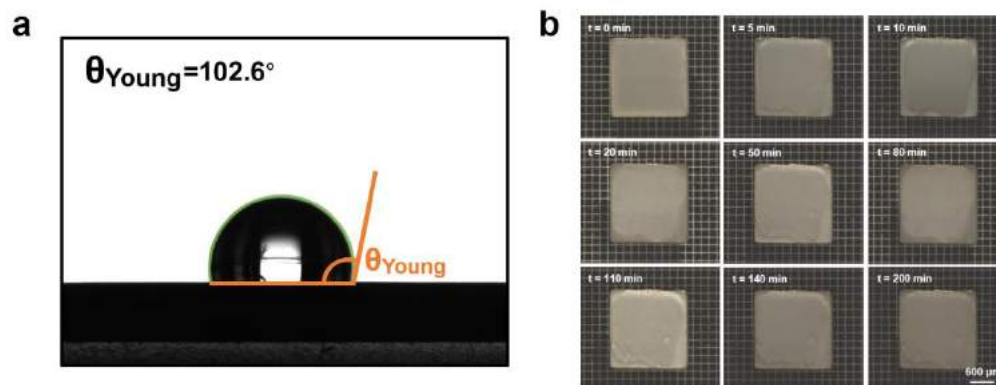
Figure S1
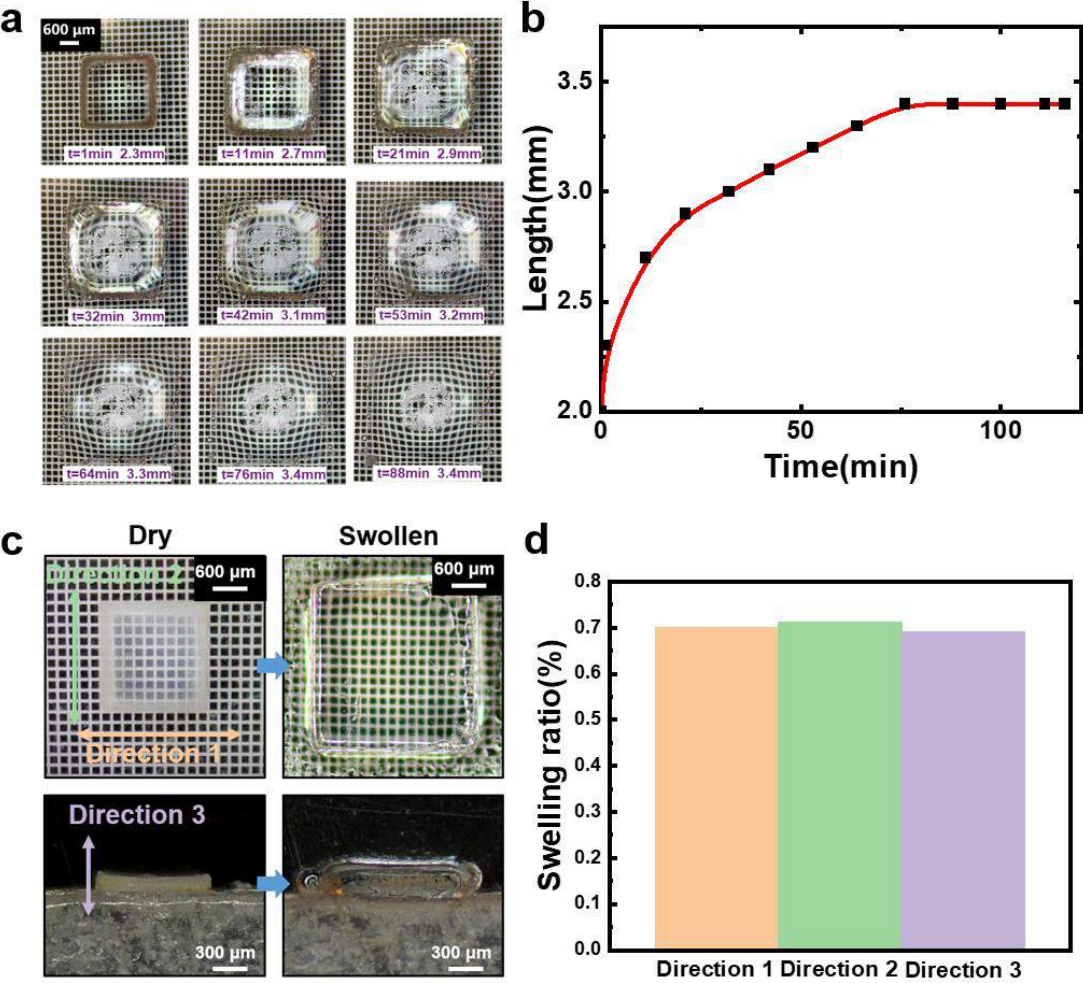
Figure S1. Swelling behaviors of PVA in water. a) Swelling process of PVA film with a size of 2*2*0.18 mm. b) Variation of the edge length of PVA film over time. c) Photo of swelling of PVA film in three directions. d) The swelling rate of the PVA film in three directions.
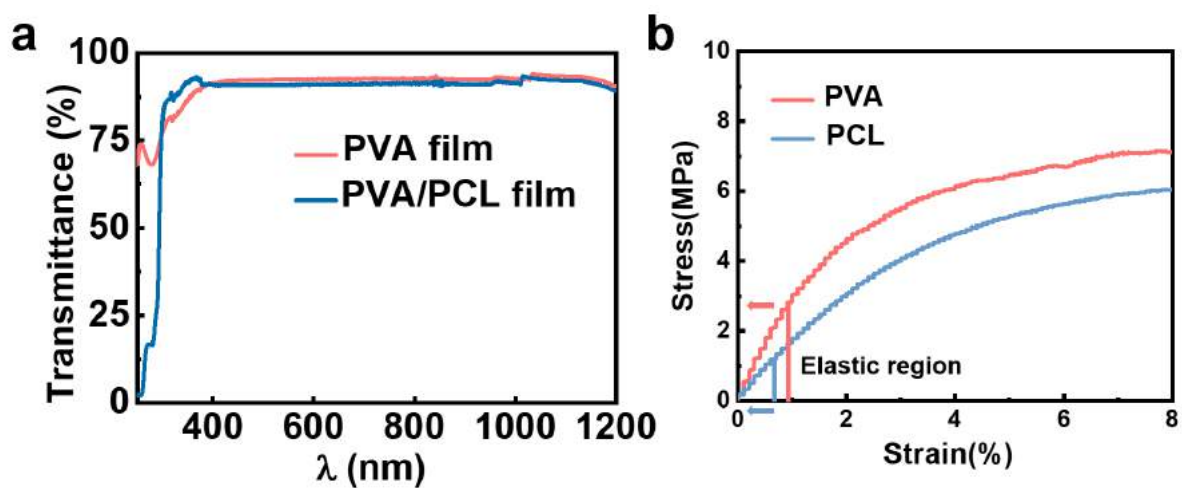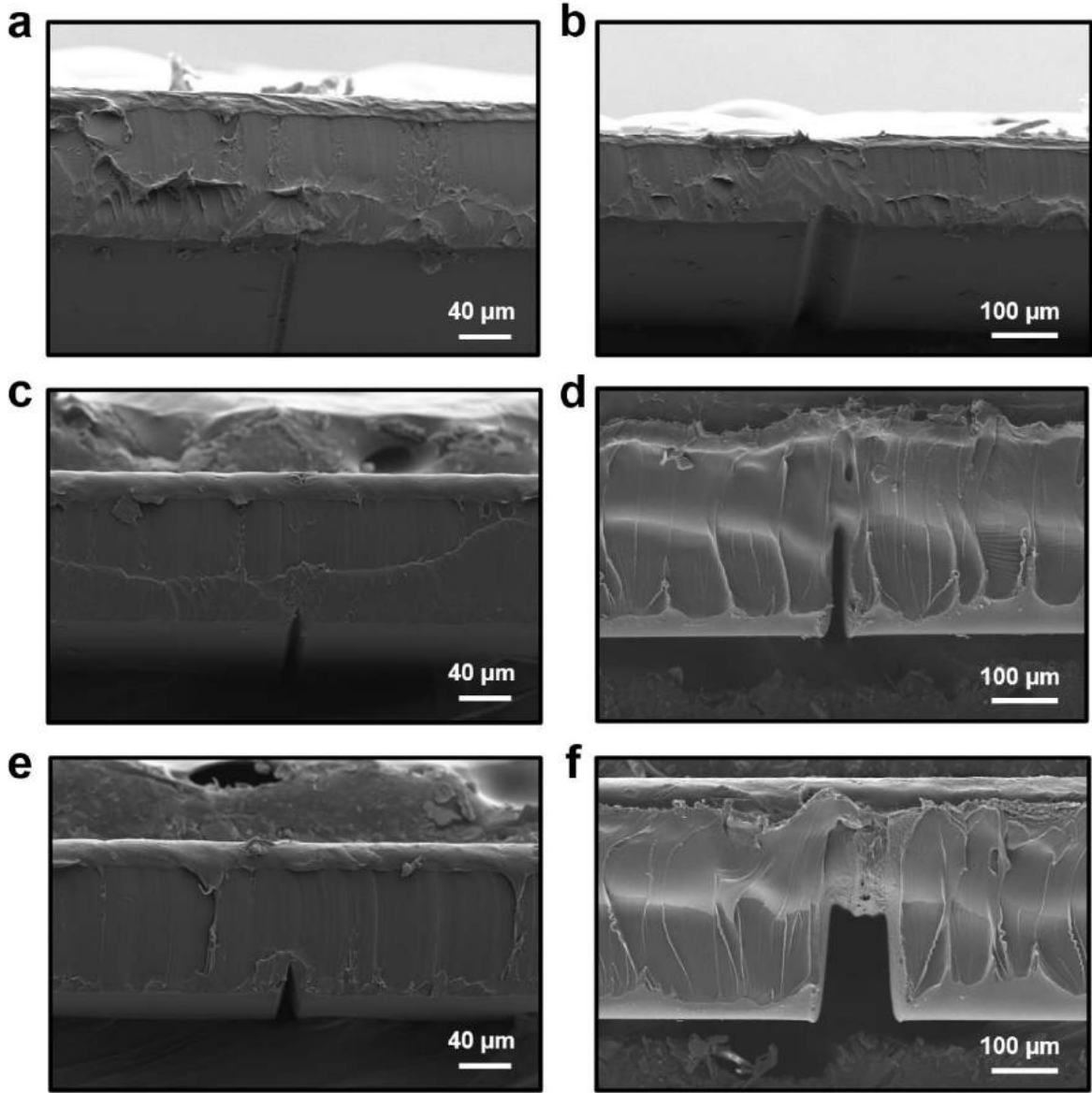
Figure S2

Figure S2. The hydrophobicity of PCL. a) The water contact angle of the PCL film. b) Immersion of PCL film with a size of 2*2*0.2 mm in water.
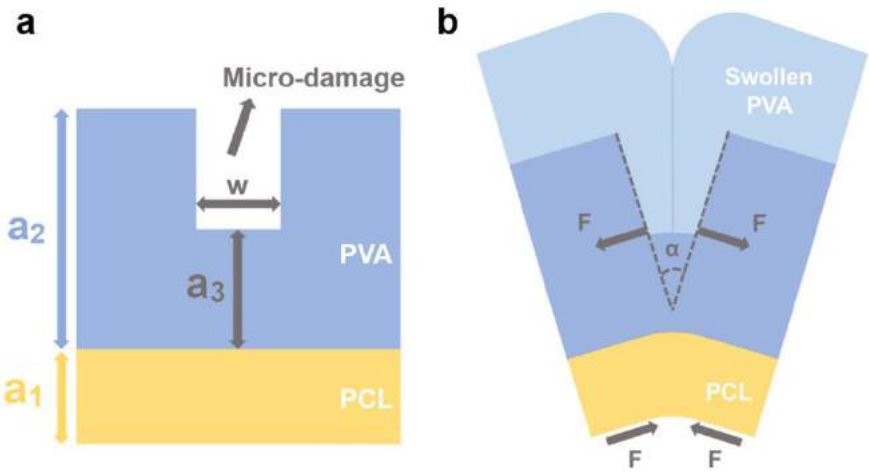
Figure S3

Figure S3. Optical and mechanical properties of bilayers. a) The light transmission performance of the double-layer structure. b) Mechanical properties of PVA film and PCL film.

Figure S4

Figure S4. Microdamage of different depths and widths formed by changes in laser processing processes.

Figure S5

Figure S5. Schematic diagram of bending model of bilayer structure with micro-damage.

Figure S6
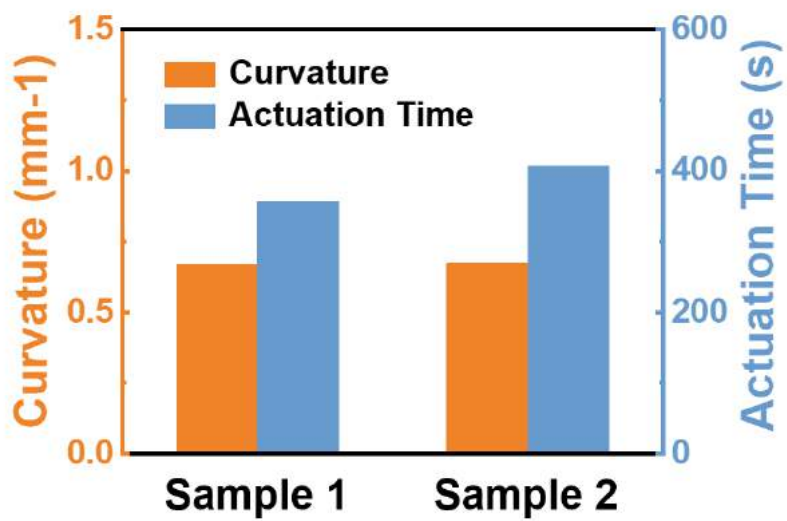
Figure S6. The independent control of actuation time.

Figure S7
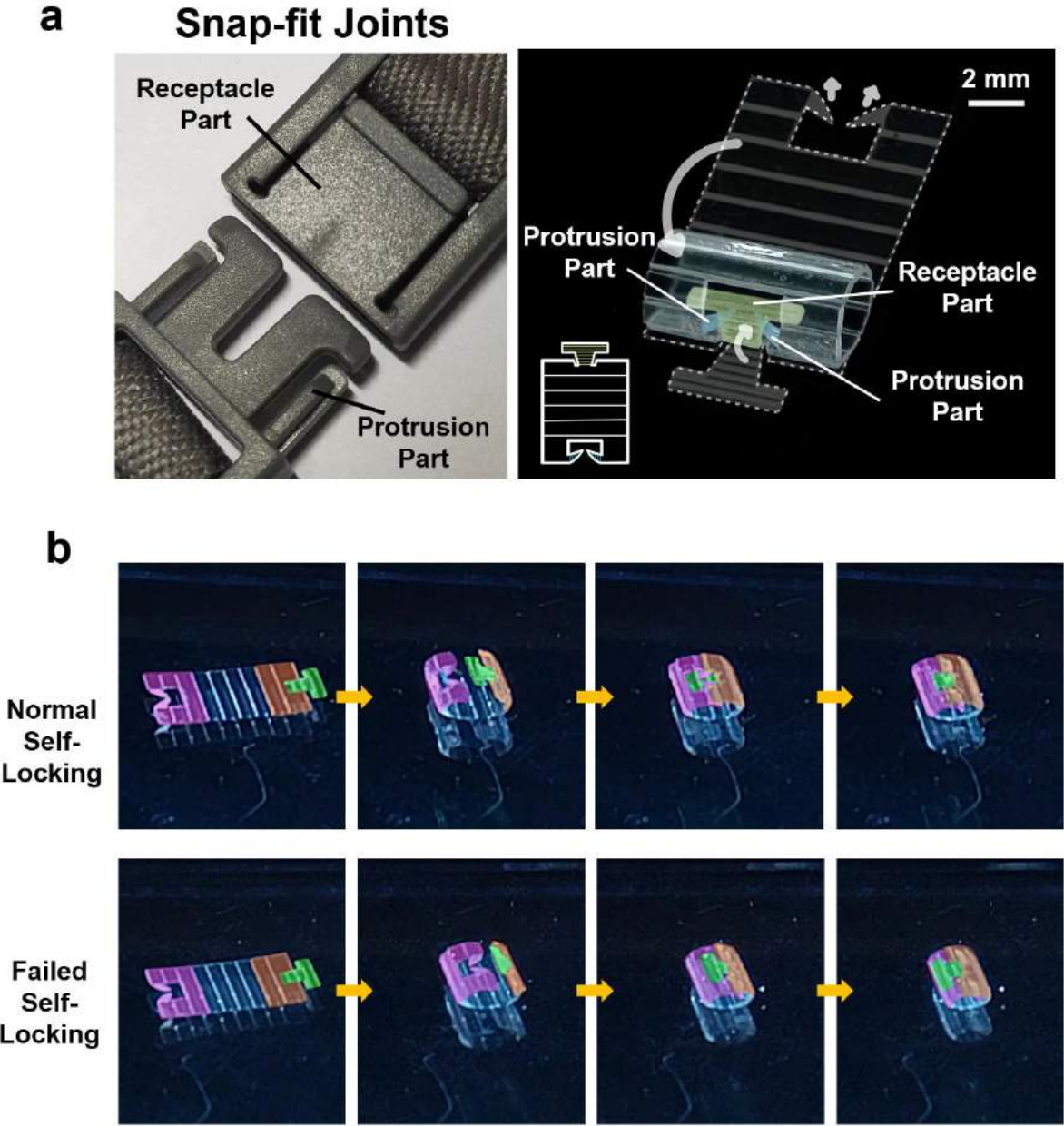
Figure S7. The formation process of the self-locking structure. a) Detailed illustrations for components of the self-locking structure. b) The action process of a normal self-locking structure and a failed self-locking structure.

Figure S8
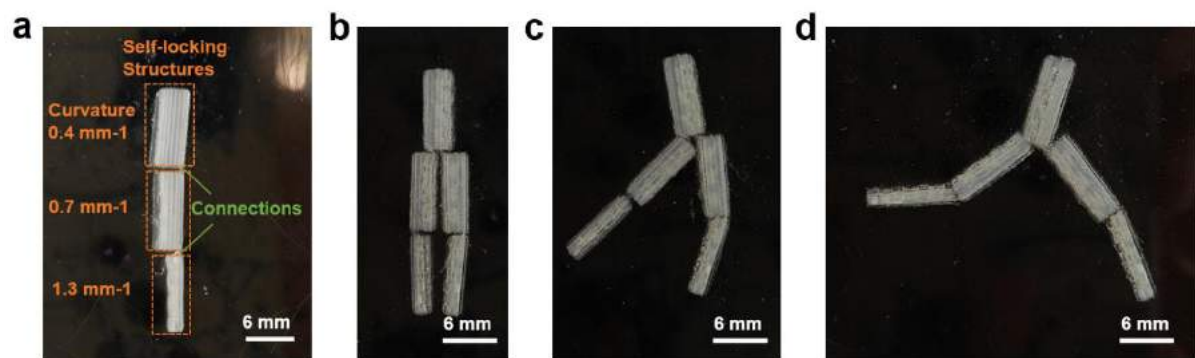
Figure S8. Patterns formed by interconnecting Self-locking structures with different self-locking curvatures on one film.

Figure S9
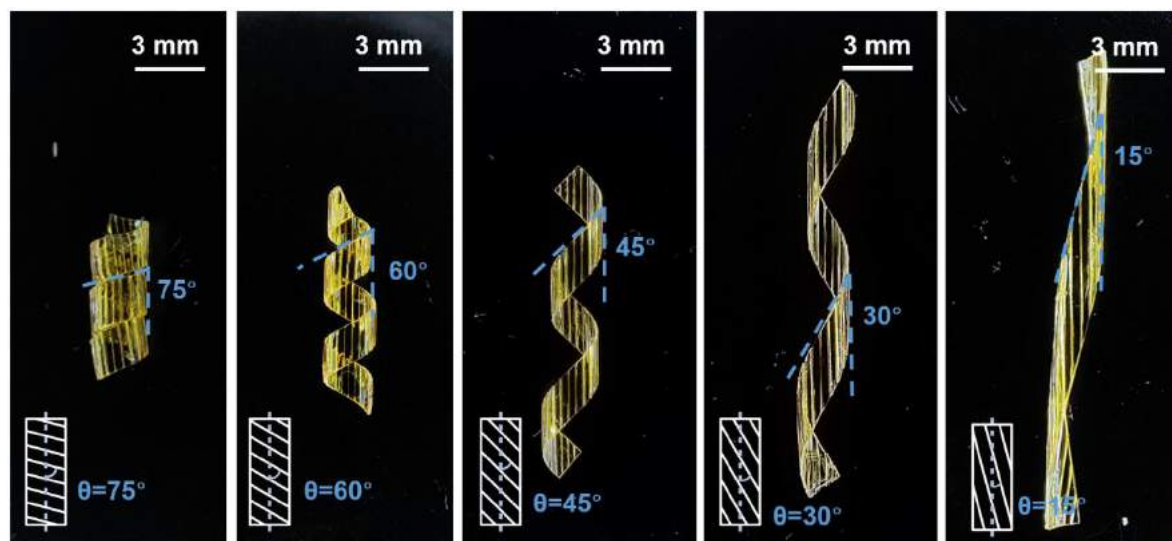
**Figure S9.** Regulation of the action of PI/PVA bilayers.

Figure S10
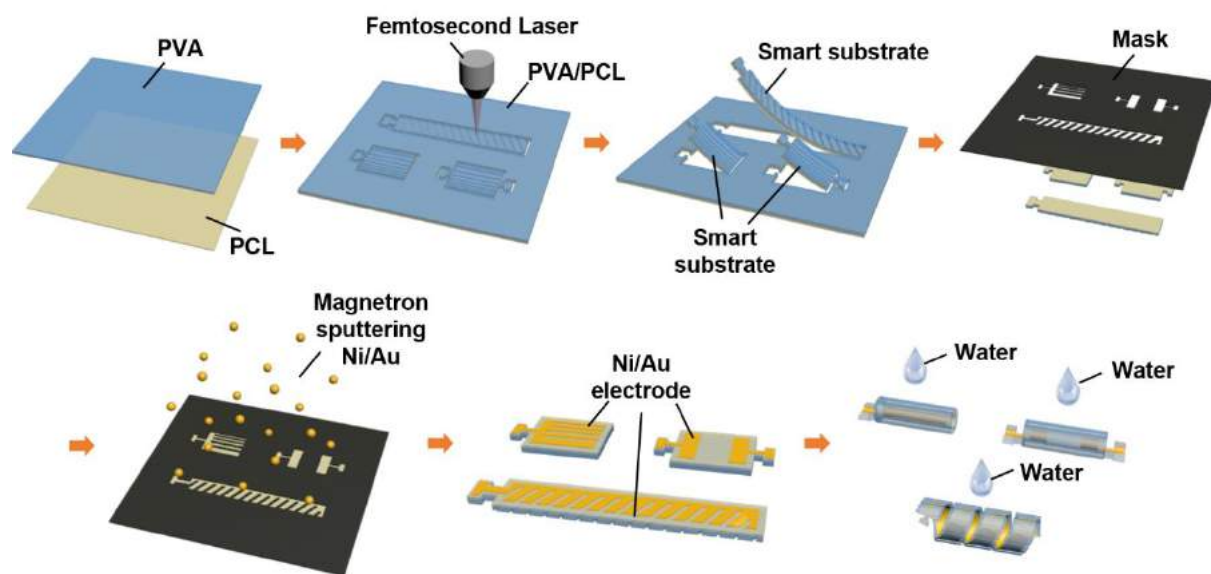
Figure S10. Fabrication process of the spiral wound electrode and the designed shapeshifting of the electrode in water.

Figure S11
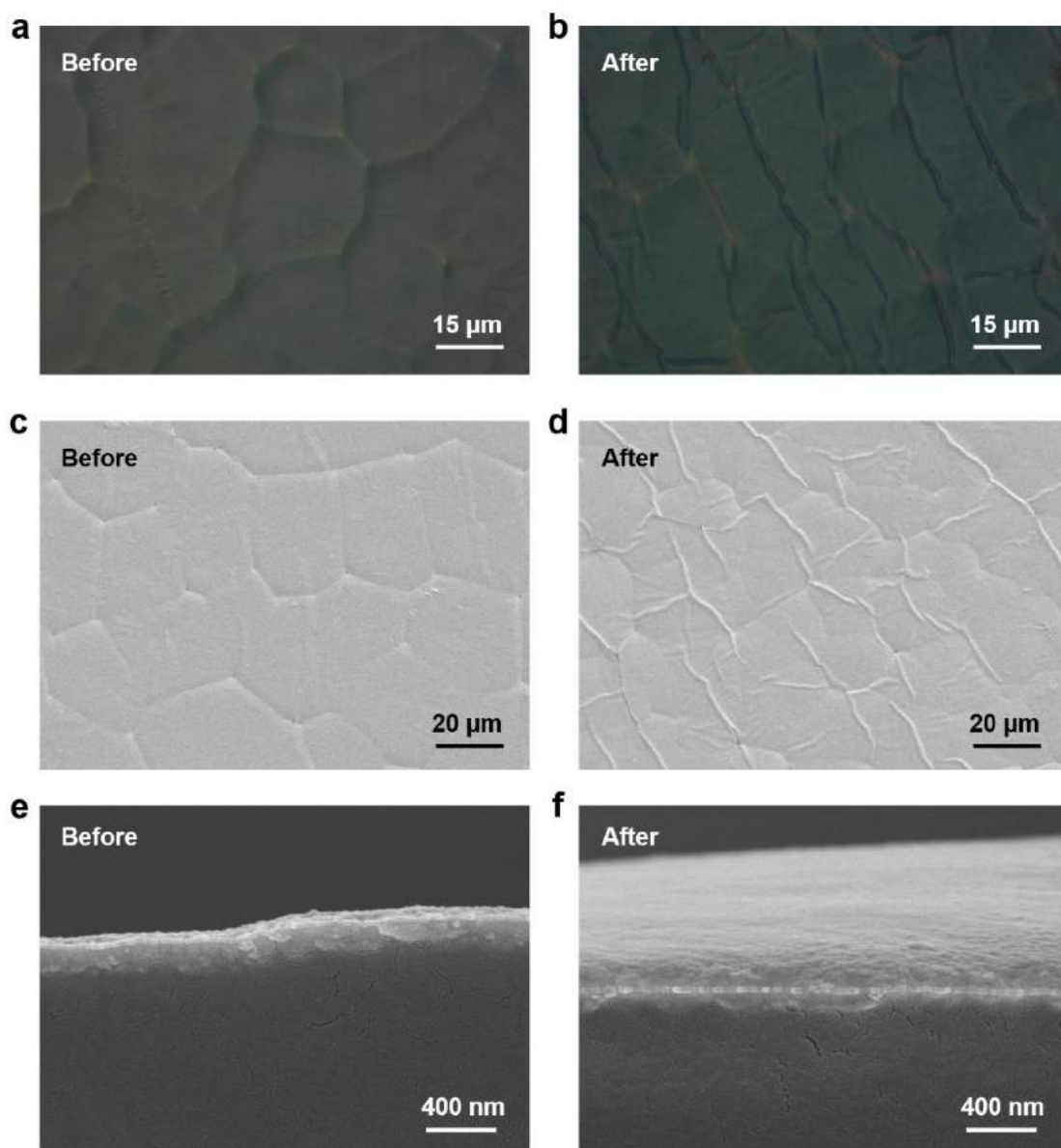
Figure S11. Gold nanofilm and the interface between the gold nanofilm and PCL before and after bending. Optical image of the gold nanofilm surface a) before, and b) after bending. SEM image of the gold nanofilm surface c) before, and d) after bending. SEM image (cross-sectional view) of the interface between the gold nanofilm and PCL e) before, and f) after bending.

Figure S12
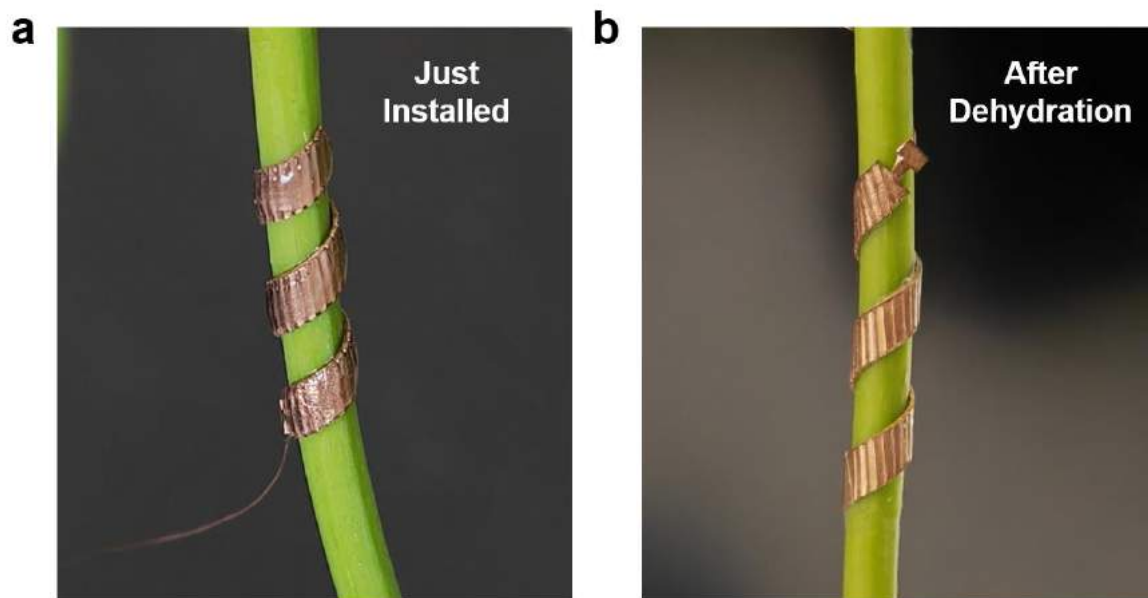
Figure S12. The spiral twining electrode before and after dehydration of PVA.

Figure S13

Figure S13. A cylinder with an inner diameter of approximately 100 μm and an outer diameter of approximately 200 μm.

Table S1

No.	Materials of substrate	Bio-interfaces	Biodegradable	Stimulus	Shape	Process for regulating deformation	Adjustable deformation parameters	Compatible with traditional 2D processes	Ref.
1	Shape memory polymer	Peripheral nerve electrode	No	Thermal (37°C)	Twining	Molds	Direction, Curvature	No	[1]
2	Shape memory polymer	Scaffolds	No	Thermal (37°C)	Tubular shape	Molds	Curvature	/	[2]
3	Flex resin	Spinal cord electrode	No	Air pressure	Paddle-type	Photolithographic	/	No	[3]
4	Flex resin	Peripheral nerve electrode	No	Water	Folded ribbon	3D printing	Curvature	No	[4]
5	Hydrogel	Monitoring the motions of organs	No	Water	X-shaped	Photolithographic	Direction	No	[5]
6	Hydrogel	Regenerative neuronal cuff	No	Solution composition and pH	Microtube	Photolithographic	Curvature	Yes	[6]
Our work	Xerogel	Plant electrophysiological electrode, Peripheral nerve electrode	Yes	Water	Tubular / Twining/ self-locking	Laser scribing process	Direction (the error within ±3°), Curvature, Actuation time	Yes	/

Table S1. The performance comparison of stimuli-responsive deformable substrate for bio-interfaces.

1. Zhang, Y.; Zheng, N.; Cao, Y.; Wang, F.; Wang, P.; Ma, Y.; Lu, B.; Hou, G.; Fang, Z.; Liang, Z.; Yue, M.; Li, Y.; Chen, Y.; Fu, J.; Wu, J.; Xie, T.; Feng, X., Climbing-inspired twining electrodes using shape memory for peripheral nerve stimulation and recording. **2019,** *5* (4), eaaw1066.
2. Zhao, Q.; Wang, J.; Cui, H.; Chen, H.; Wang, Y.; Du, X., Programmed Shape-Morphing Scaffolds Enabling Facile 3D Endothelialization. *Advanced Functional Materials* **2018,** *28* (29).

3. Woodington, B. J.; Curto, V. F.; Yu, Y.-L.; Martínez-Domínguez, H.; Coles, L.; Malliaras, G. G.; Proctor, C. M.; Barone, D. G., Electronics with shape actuation for minimally invasive spinal cord stimulation. **2021,** *7* (26), eabg7833.

4. Hiendlmeier, L.; Zurita, F.; Vogel, J.; Del Duca, F.; Al Boustani, G.; Peng, H.; Kopic, I.; Nikic, M.; T, F. T.; Wolfrum, B., 4D-Printed Soft and Stretchable Self-Folding Cuff Electrodes for Small-Nerve Interfacing. *Adv Mater* **2023,** *35* (12), e2210206.

5. Hao, X. P.; Li, C. Y.; Zhang, C. W.; Du, M.; Ying, Z.; Zheng, Q.; Wu, Z. L., Self-Shaping Soft Electronics Based on Patterned Hydrogel with Stencil-Printed Liquid Metal. *Advanced Functional Materials* **2021,** *31* (47).

6. Karnaushenko, D.; Munzenrieder, N.; Karnaushenko, D. D.; Koch, B.; Meyer, A. K.; Baunack, S.; Petti, L.; Troster, G.; Makarov, D.; Schmidt, O. G., Biomimetic Microelectronics for Regenerative Neuronal Cuff Implants. *Adv Mater* **2015,** *27* (43), 6797-805.

Table S2

| parameters	value	description
E_1 (MPa)	100	Young's modulus of PCL (tested)
E_2 (MPa)	200	Young's modulus of PVA (tested)
E_3 (MPa)	0.07	Young's modulus of PVA gel after water swelling (calculated)
D (mm/mm)	0.7	linear expansion rate of the PVA (tested)

Table S2. Parameters in the Model.

Movie S1
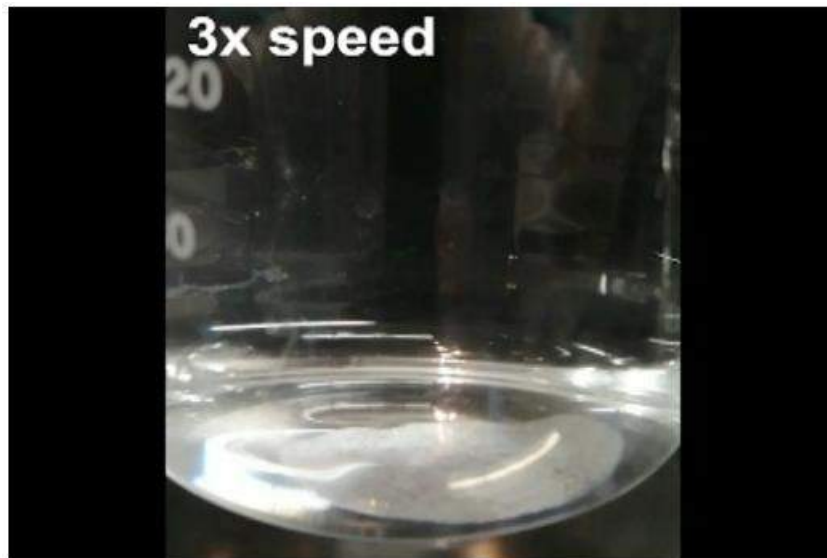
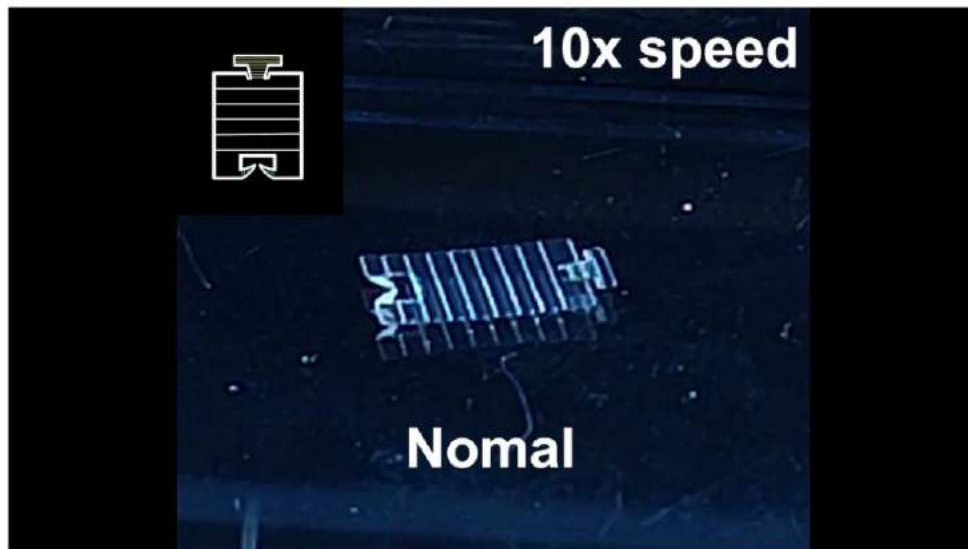**Movie S1.** Formation of a three-dimensional concatenated structure containing three helical segments.

Movie S2
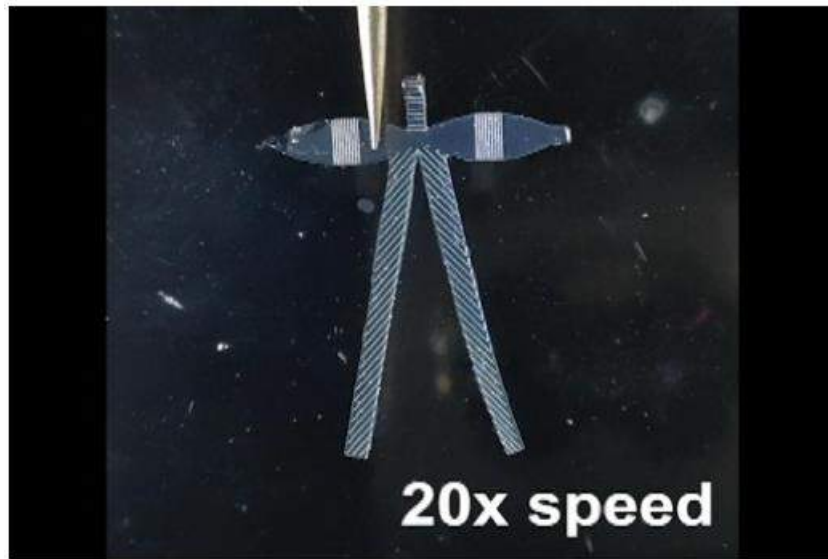
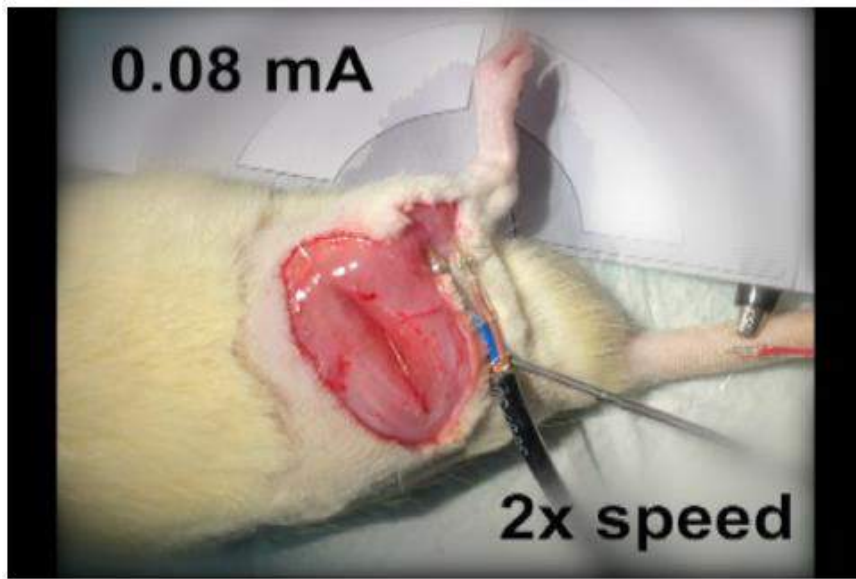**Movie S2.** Formation of a bowknot shape.

Movie S3

Movie S3. Formation of the self-locking structure.

Movie S4

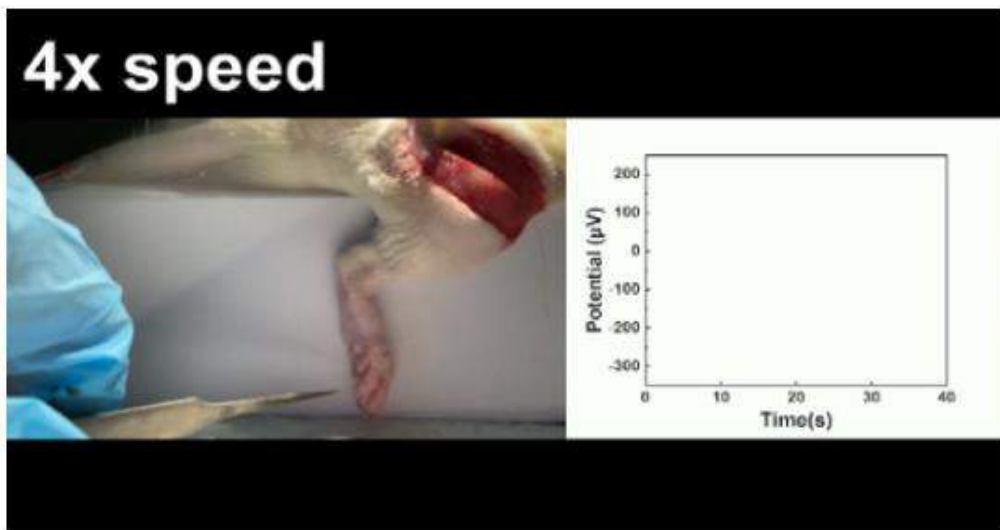

Movie S4. The process of mounting helical electrodes onto plant stems.

Movie S5

Movie S5. Movement of the hindlimb during electrical stimulation using self-deforming electrodes.

Movie S6

Movie S6. Composite nerve signals generated by mechanical stimulation of hindlimbs.